

# Spin Frustration in Antiperovskite Systems: $(\text{TTF}^{\bullet+} \text{ or } \text{TSF}^{\bullet+})_3[(\text{Mo}_6\text{X}_{14})^{2-}\text{Y}^-]$

Takaaki Hiramatsu,<sup>\*a</sup> Yukihiro Yoshida,<sup>a</sup> Gunzi Saito,<sup>\*a,b</sup> Akihiro Otsuka,<sup>c</sup> Hideki Yamochi,<sup>c</sup> Yasuhiro Shimizu,<sup>d</sup> Yuma Hattori,<sup>e</sup> Yuto Nakamura,<sup>e</sup> Hideo Kishida,<sup>e</sup> Hiroshi Ito,<sup>e</sup> Kaplan Kirakci,<sup>f,‡</sup> Stéphane Cordier,<sup>f</sup> and Christiane Perrin<sup>f</sup>

<sup>a</sup> Faculty of Agriculture, Meijo University, 1-501 Shiogamaguchi, Tempaku-ku, Nagoya 468-8502, Japan

<sup>b</sup> Toyota Physical and Chemical Research Institute, 41-1, Yokomichi, Nagakute, Aichi 480-1192, Japan

<sup>c</sup> Research Center for Low Temperature and Materials Sciences, Kyoto University, Sakyo-ku, Kyoto 606-8501, Japan

<sup>d</sup> Department of Physics, Graduate School of Science, Nagoya University, Nagoya 464-8602, Japan

<sup>e</sup> Department of Applied Physics, Nagoya University, Chikusa-ku, Nagoya 464-8603, Japan

<sup>f</sup> Institut des Sciences Chimiques de Rennes, UMR CNRS 6226, Université de Rennes 1, Avenue du Général Leclerc, 35042 Rennes cedex, France

---

Present address ‡ Institute of Inorganic Chemistry of the Academy of Sciences of the Czech Republic

Corresponding authors Takaaki Hiramatsu; E-mail: htakaaki@meijo-u.ac.jp

Gunzi Saito; E-mail: gsaito@meijo-u.ac.jp

## Abstract

Two novel antiperovskite charge-transfer (CT) solids composed of a tetraselenafulvalene radical cation ( $\text{TSF}^{\bullet+}$ ), dianionic molybdenum cluster unit  $[\text{Mo}_6\text{X}_{14}]^{2-}$ , and halogen anion ( $\text{Y}^-$ ) ( $\text{X}, \text{Y} = \text{Cl}, \text{Br}$ ) were prepared by electrocrystallization. Their crystal structures and magnetic properties with regard to spin frustration are discussed together with those of isostructural tetrathiafulvalene (TTF) CT solids previously reported. Both TSF and TTF salts have an apex sharing distorted octahedral spin lattice with a rhombohedral  $R\bar{3}$  space group. The calculated overlap integrals based on the crystal structures and insulating nature of the TSF salts indicate that they are Mott insulators. Their spin susceptibilities obeyed the Curie–Weiss law and exhibited an antiferromagnetic ordering at lower temperatures for the TSF salts (Néel temperature,  $T_N = 3.0$  K for  $\text{X} = \text{Y} = \text{Cl}$  and 5.5 K for  $\text{X} = \text{Y} = \text{Br}$ ) than the TTF salts. The Curie–Weiss temperatures ( $|\Theta_{\text{CW}}| \sim 1.6\text{--}6.3$  K) for the TSF salts are lower than those of the TTF salts. For the TSF salts, spin-flop behavior was detected at 3.2 T for  $\text{X} = \text{Y} = \text{Cl}$  and 1.5 T for  $\text{X} = \text{Y} = \text{Br}$  at 1.9 K. Due to both the distortion of the octahedral geometry of the spin lattice and the anisotropic molecular orientation, the geometrical spin frustrations in TSF and TTF systems are weakened.

## 1. Introduction

Geometrical spin frustration suppresses classical long-range magnetic ordering of the Néel state and allows novel quantum states such as the quantum spin liquid (QSL) state to exist in two-dimensional (2D)  $S = 1/2$  antiferromagnets, as proposed by Anderson.<sup>[1]</sup> Such systems have been theoretically predicted to have a ground state with many degenerate states.<sup>[2]</sup> To obtain spin-frustrated materials, the geometries of competing spin lattices are crucial. Triangular, kagome, pyrochlore, tetrahedral, octahedral, and

hyperkagome, which is a three-dimensional (3D) version of kagome, spin lattices have previously been discussed (Fig. 1).<sup>[3]</sup> In some cases, a compromise non-frustrated spin configuration such as a spiral (120°) or collinear order for triangle<sup>[4]</sup> and 109° for tetrahedron spin lattice,<sup>[3b]</sup> are discussed.

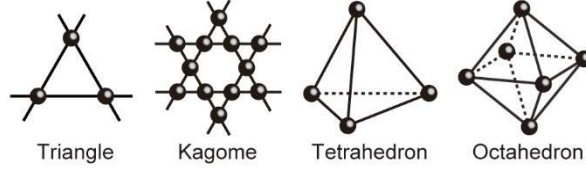


Fig. 1. Geometries of spin lattices having strong spin frustration.

The Curie–Weiss temperature ( $\Theta_{CW}$ ) is a parameter that determines the capability of accessing the QSL state, with the absolute value of  $\Theta_{CW}$  increasing upon increasing the magnetic exchange interaction  $|J|$ .  $J$  is represented by Eq. 1,

$$J \approx -4t^2/U \quad (1)$$

where  $t$  and  $U$  are the transfer interaction and effective on-site Coulomb repulsion energy, respectively. The frustration index ( $f$ ) is defined by Eq. 2, where  $T_m$  is the temperature at which magnetic order occurs, was proposed as a measure of spin frustration. When  $f > 10$ , this is thought to indicate a system with strong spin frustration,<sup>[3a,5]</sup> while a real QSL system should have  $f \sim \infty$ .

$$f = -\Theta_{CW} / T_m \quad (2)$$

However, almost no QSL systems have been obtained for materials with a large spin quantum number ( $S > 1/2$ ), even though the geometry of the spin lattice is triangular or kagome with strong spin frustration.<sup>[3,6]</sup> The first QSL system is a dimer-type Mott insulator  $\kappa$ -(ET)<sub>2</sub>Cu<sub>2</sub>(CN)<sub>3</sub>,<sup>[7a]</sup> which is a charge-transfer (CT) solid between an electron donor ET (Fig. 2a; bis(ethylenedithio)tetrathiafulvalene) and a counteranion Cu<sub>2</sub>(CN)<sub>3</sub><sup>1-</sup>. An ET dimer has a +1 charge and a spin value of 1/2. The localized spins on ET dimers of  $\kappa$ -(ET)<sub>2</sub>Cu<sub>2</sub>(CN)<sub>3</sub> form a nearly equilateral triangular lattice in terms of interdimer transfer interactions ( $t'/t = 1.09$ , Fig. 2b). The QSL state was confirmed by NMR spectroscopy, spin susceptibility, and  $\mu$ SR measurements down to 20 mK ( $|J|/k_B = 250$  K,  $|\Theta_{CW}| = 375$  K,  $f > 1.8 \times 10^4$ ).<sup>[7a,b,d]</sup> Since the discovery of the QSL state in  $\kappa$ -(ET)<sub>2</sub>Cu<sub>2</sub>(CN)<sub>3</sub>, several materials based on triangular or kagome lattices were reported to have such a spin state.<sup>[8-10]</sup> Some examples include EtMe<sub>3</sub>Sb[Pd(dmit)<sub>2</sub>]<sub>2</sub> (triangular spin lattice, dmit: 4,5-dimercapto-1,3-dithiole-2-thione,  $S = 1/2$ ,  $t'/t \sim 0.9$ ,  $|J|/k_B = 220$ –250 K,  $|\Theta_{CW}| = 325$ –375 K,  $f > 1.6 \times 10^4$ ),<sup>[11]</sup>  $\kappa$ -H<sub>3</sub>(Cat-EDT-TTF)<sub>2</sub> (triangular spin lattice, H<sub>2</sub>(Cat-EDT-TTF): catechol-fused ethylenedithiotetrathiafulvalene,  $S = 1/2$ ,  $t'/t \sim 1.48$ ,  $|J|/k_B = 80$ –100 K,  $|\Theta_{CW}| = 120$ –150 K,  $f > 2.4 \times 10^3$ ),<sup>[12]</sup> ZnCu<sub>3</sub>(OH)<sub>6</sub>Cl<sub>2</sub> (kagome spin lattice,  $S = 1/2$ ,  $|J|/k_B = 197$  K,  $|\Theta_{CW}| \sim 300$  K,  $f > 8.9 \times 10^3$ ),<sup>[13]</sup> and Na<sub>4</sub>Ir<sub>3</sub>O<sub>8</sub> (hyperkagome spin lattice,  $|J|/k_B = 300$  K,  $S = 1/2$ ,  $|\Theta_{CW}| = 650$  K,  $f > 325$ ).<sup>[14]</sup> Only the QSL state of  $\kappa$ -(ET)<sub>2</sub>Cu<sub>2</sub>(CN)<sub>3</sub> neighbors to superconducting state among them.<sup>[7c,e]</sup> Recently we added new candidate  $\kappa$ -(ET)<sub>2</sub>B(CN)<sub>4</sub> with triangular spin lattice ( $t'/t = 1.42$ ,  $S = 1/2$ ) which exhibits quantum critical behavior over a wide temperature range 5–100 K and undergoes a transition to a valence bond crystal ground state below 5 K.<sup>[15]</sup>

Based on the crystal and band structures and transport properties, we have proposed the following requirements (A–F) for designing principle of the materials with a QSL state next to a superconducting state for  $\kappa$ -(ET)<sub>2</sub>X: [A] small  $S$  value ( $S = 1/2$ ); [B] the system should be a Mott insulator ( $W < 0.57$  eV and  $U/W$

$> 0.89$  at room temperature (RT) for ET systems, where  $W$  is the width of upper HOMO band); [C] the Mott insulating state has a partial CT state close to the itinerant region; [D] the spin lattice should have a geometry which exerts strong geometrical frustration ( $t'/t > 0.9$  for triangular spin lattice); [E] high  $|\mathcal{O}_{CW}|$ , high  $|J|$ , and high  $f$  values are required to observe the QSL state at the experimentally available temperature; and [F] the material must maintain weak energy dispersion along the weakest direction in the case of magnetic interactions of the 2D system.<sup>[16]</sup>

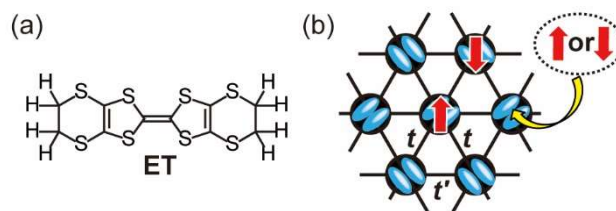


**Fig. 2.** (a) Chemical structure of ET. (b) Schematic view of the triangular spin lattice of a dimer-type Mott insulator of  $\kappa$ -(ET)<sub>2</sub>X. Cyan ellipsoids are ET molecules and black circles represent one spin site of the ET dimer.  $t$  and  $t'$  are interdimer transfer integrals, with  $t'/t$  representing the shape of the triangular spin lattice. Red arrows indicate spins.

Since tetragonal and octahedral spin lattices have high potential for geometrical spin frustration, examination of these spin lattices is very important for further development of QSL systems. Thus far, tetragonal and octahedral spin lattices have been very limited in organic solids, whereas several systems are known in inorganic solids. With regard to the tetragonal spin lattice, pyrochlore (e.g., Na<sub>4</sub>I<sub>3</sub>O<sub>8</sub>) and B-site spinel (e.g., ZnCr<sub>2</sub>O<sub>4</sub>:  $S = 3/2$ ,  $|\mathcal{O}_{CW}| = 390$  K,  $T_N = 16$  K,  $f = 24$ ) are representative systems, where  $T_N$  is the Néel temperature.<sup>[3a]</sup> For the octahedral spin lattice, octahedral solid Na<sub>3</sub>[Co<sub>6</sub>O(OH)(C<sub>8</sub>H<sub>4</sub>O<sub>4</sub>)<sub>6</sub>]H<sub>2</sub>O (C<sub>8</sub>H<sub>4</sub>O<sub>4</sub>: isophthalate dianion) is known to have a high  $|\mathcal{O}_{CW}|$  (118.5 K),<sup>[17]</sup> whereas cubic antiperovskite manganese Mn<sub>3</sub>AX (A: transition metal and semiconductive element, X: C or N) are known to have large negative thermal expansion at the  $T_N$  with a peculiar noncollinear magnetic structure.<sup>[18]</sup> Batail et al. reported that the tetrathiafulvalene (TTF, **Fig. 3a**) cation radical molecule TTF<sup>•+</sup> afforded an antiperovskite (octahedral) spin lattice with cluster anions [Re<sub>6</sub>Se<sub>5</sub>Cl<sub>9</sub>]<sup>2-</sup><sup>[19a]</sup> or [Mo<sub>6</sub>X<sub>14</sub>]<sup>2-</sup><sup>[19b]</sup> and a halogen anion (Y<sup>-</sup>). In the case of the [Mo<sub>6</sub>X<sub>14</sub>]<sup>2-</sup> cluster unit, there have been four CT solids formulated as (TTF<sup>•+</sup>)<sub>3</sub>[(Mo<sub>6</sub>X<sub>14</sub>)Y] (X = Y = Cl; X = Br, Y = Cl, Br, I), where the six molybdenum atoms form an octahedron, eight X atoms occupy the X<sup>i</sup> sites (i: inner), and the latter six atoms are positioned in the X<sup>a</sup> sites (a: apical) (**Figs. 3b, 3c**). Although these solids exhibit antiferromagnetic (AF) ordering at 6.2–8.2 K with weak frustration ( $f = 1.5$ –2.0), to the best of our knowledge, they are the unique examples of organic octahedral spin lattices. Here, we extended the study of the octahedral spin lattice using tetraselenafulvalene (TSF, **Fig. 3a**) and obtained (TSF)<sub>3</sub>[(Mo<sub>6</sub>Cl<sub>14</sub>)Cl] (**1**) and (TSF)<sub>3</sub>[(Mo<sub>6</sub>Br<sub>14</sub>)Br] (**2**), which were isostructural solids with increased overlap integrals ( $\propto t$ ). We also examined the spin frustration in these crystals based on the above requirements for a QSL system.

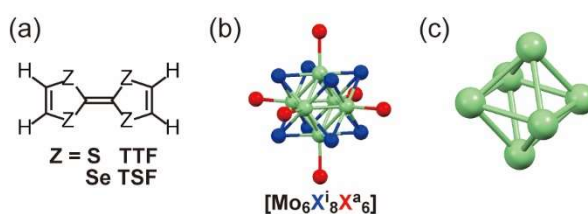


**Fig. 3.** (a) TTF and TSF molecules. (b) [Mo<sub>6</sub>X<sub>8</sub>X<sup>a</sup><sub>6</sub>]<sup>2-</sup> cluster unit. Mo: pale green, face-capped inner halogens (X<sup>i</sup>): blue, terminal apical halogens (X<sup>a</sup>): red. (c) Mo<sub>6</sub> skeleton in a [Mo<sub>6</sub>X<sub>8</sub>X<sup>a</sup><sub>6</sub>]<sup>2-</sup> cluster unit.

## 2. Experimental

### 2.1 Electrocrystallization

Electrooxidation of TSF in the presence of  $(\text{TBA})_2[\text{Mo}_6\text{X}_{14}]$  (TBA: tetrabutylammonium) and  $\text{TBA}\cdot\text{Y}$  ( $\text{X} = \text{Y} = \text{Cl}, \text{Br}, \text{I}$ ) afforded antiperovskite compounds  $(\text{TSF})_3[(\text{Mo}_6\text{X}_{14})\text{Y}]$  for  $\text{X} = \text{Y} = \text{Cl}$  and  $\text{Br}$ , but not for  $\text{X} = \text{Y} = \text{I}$ . Typically, TSF (40  $\mu\text{mol}$ ) was added to the anodic compartment, whereas  $(\text{TBA})_2[\text{Mo}_6\text{X}_{14}]$ <sup>[20]</sup> (25  $\mu\text{mol}$ ) and  $\text{TBA}\cdot\text{X}$  (25  $\mu\text{mol}$ ) were added to the cathodic compartment. After being dissolved in acetonitrile (*ca.* 18 mL), a constant current (1.0  $\mu\text{A}$ ) was passed between the two platinum electrodes for approximately one month to afford black, shiny rhombohedral crystals of  $(\text{TSF})_3[(\text{Mo}_6\text{Cl}_{14})\text{Cl}]$  (**1**) and  $(\text{TSF})_3[(\text{Mo}_6\text{Br}_{14})\text{Br}]$  (**2**) (typically  $0.1 \times 0.1 \times 0.1 \text{ mm}^3$  in size). Other polymorphs with the same space group (rhombohedral  $R\bar{3}$ ) but larger unit cells than those of the antiperovskite systems were also harvested as black crystals for  $\text{X} = \text{Cl}, \text{Br}$ , and  $\text{I}$ ; however, only the  $[\text{Mo}_6\text{X}_{14}]$  cluster units were crystallographically refined and the  $\text{Y}$  content was unknown. In addition,  $(\text{TSF})\text{X}(\text{H}_2\text{O})$  was obtained as a purple crystal for  $\text{X} = \text{Cl}$ . The antiperovskite phases were isolated under a microscope.  $(\text{TTF})_3[(\text{Mo}_6\text{Br}_{14})\text{Br}]$  was also prepared according to Ref. 19b.

### 2.2 Measurements

Single-crystal X-ray diffraction data were collected on a CCD-type diffractometer (Bruker SMART APEX II for 300 K and 100 K and Rigaku Mercury CCD for 25 K) with graphite-monochromated MoK $\alpha$  radiation ( $\lambda = 0.71073 \text{ \AA}$ ). The crystal structures were solved by a direct method using SHELXS<sup>[21]</sup> and refined by a full-matrix least-squares method on  $F^2$  using SHELXL.<sup>[21]</sup> The crystallographic data and refinement parameters are summarized in Table S1 for **1**, Table S2 for **2**, and Table S3 for  $(\text{TTF})_3[(\text{Mo}_6\text{Br}_{14})\text{Br}]$ . The CIF files, CCDC 999368 (300 K), 999367 (100 K), and 999366 (25 K) for **1**, 999365 (300 K), 999364 (100 K), and 999363 (25 K) for **2**, 999370 (300 K), and 999369 (100 K) for  $(\text{TTF})_3[(\text{Mo}_6\text{Br}_{14})\text{Br}]$ , can be obtained free of charge from The Cambridge Crystallographic Data Centre via [www.ccdc.cam.ac.uk/data\\_request/cif](http://www.ccdc.cam.ac.uk/data_request/cif).

The direct current conductivity was measured using a standard four-probe technique with platinum wires ( $\phi$  20  $\mu\text{m}$ ) attached to a single crystal with carbon paint (DOTITE XC-12).

A Quantum Design MPMS-XL superconducting quantum interference device (SQUID) magnetometer was used to collect magnetic susceptibility data for polycrystalline samples between 1.9 and 300 K at 0.1–5.0 T. Core diamagnetism values were estimated based on the sum of Pascal's constants (in  $\text{emu mol}^{-1}$ ) for halogen anion  $\text{Y}^-$  ( $-0.26 \times 10^{-4}$  for  $\text{Cl}^-$  and  $-0.36 \times 10^{-4}$  for  $\text{Br}^-$ ) and from the measured value for  $\text{TSF}$ <sup>[22]</sup> ( $-1.27 \times 10^{-4}$ ) and Mo clusters ( $-2.15 \times 10^{-4}$  for  $[\text{Mo}_6\text{Cl}_{14}]^{2-}$ <sup>[23]</sup> and  $-2.62 \times 10^{-4}$  for  $[\text{Mo}_6\text{Br}_{14}]^{2-}$ <sup>[24]</sup>).  $^1\text{H}$  NMR spectroscopic measurements were conducted on polycrystalline samples of **2** in a static magnetic field of 1.51 T between 4.2 and 150 K. The spectra were obtained from Fourier transformation of solid echo  $(\pi/2)_{\text{x}-\tau}-(\pi/2)_{\text{y}-\tau}$  signals. The nuclear spin-lattice relaxation rate ( $T_1^{-1}$ ) was obtained from the single-exponential nuclear magnetization recovery after the saturation comb pulses between 4.2 and 285 K. Electron paramagnetic resonance (EPR) spectra of a single crystal of **2** were recorded on a JEOL JES-TE200 X band (9 GHz) EPR spectrometer equipped with a JEOL ESCT-470 cryostat from 4.1 to 300 K.

Raman spectra were measured with an inVia Raman microscope (Renishaw) with a He-Ne laser (632.8 nm). UV-Vis-NIR spectra were measured using KBr pellets ( $3.8\text{--}40 \times 10^3 \text{ cm}^{-1}$ ) on a Shimadzu

UV-3100 spectrophotometer. FT-IR spectra were measured using KBr pellets on a Shimadzu Prestige 21 spectrophotometer in the region of 380–7800 cm<sup>-1</sup>.

### 2.3 Calculation of transfer integrals

The transfer integrals ( $t$ ) between TSF (or TTF) molecules were calculated within a tight-binding approximation using the extended Hückel molecular orbital method with single- $\zeta$  parameters, including  $d$ -orbitals of selenium (or sulfur) atoms based on the crystallographic data.<sup>[25]</sup> The HOMO of the TSF (or TTF) molecule was used as the basis function. Semi-empirical parameters for Slater-type atomic orbitals were used. The  $\zeta$ -parameters of atomic orbitals were taken from Ref. 26 for selenium and Ref. 25 for other atoms. The  $t$  values were assumed to be proportional to the overlap integral ( $S$ ) via the equation  $t = ES$  ( $E = -10$  eV).

## 3. Results and Discussion

### 3.1. Crystal structures and key-keyhole relationship

Salts **1** and **2** are isostructural to the TTF analogs and crystallize in the rhombohedral  $R\bar{3}$  space group. Table 1 summarizes the crystallographic data at RT. Figure 4a shows the crystal structure of **2**. Given that the [Mo<sub>6</sub>X<sub>14</sub>] cluster unit has a charge of -2, each TSF molecule is monocationic with  $S = 1/2$ . As such, the [(TSF<sup>+</sup>)<sub>6</sub>Br<sup>-</sup>] unit depicted in Fig. 4b is the spin lattice unit. When the center of the TSF molecule is indicated by a black circle, six black circles form an octahedral spin lattice based on the point charge approximation. The apex of the octahedron has a positive charge (antiperovskite) contrary to the negative charge in the perovskite system. **1**, **2**, and TTF analogs are approximately represented by the cubic perovskite structure composed of [(TTF<sup>+</sup> or TSF<sup>+</sup>)<sub>6</sub>(Y<sup>-</sup>)] units, as shown in Fig. 4c, where TTF or TSF are depicted by black balls, Y by orange balls, and [Mo<sub>6</sub>X<sub>14</sub>] clusters by cyan balls. The actual [(TTF<sup>+</sup> or TSF<sup>+</sup>)<sub>6</sub>(Y<sup>-</sup>)] unit possesses rhombohedral distortion and constructs a 3D framework by sharing vertices. TTF or TSF molecules have short atomic contacts with halogen Y (Fig. S1(a)) or apical halogen X<sup>a</sup> in the cluster unit (Fig. S1(b)), as summarized in Table 1.

**Table 1** Crystallographic data for (TTF or TSF)<sub>3</sub>[(Mo<sub>6</sub>X<sub>14</sub>)Y] at RT

D <sup>+</sup> a)	[Mo <sub>6</sub> X <sub>14</sub> ] <sup>2-</sup> X	Y <sup>-</sup>	$a/\text{\AA}$	$\alpha/^\circ$	$V/\text{\AA}^3$	Short atomic contact <sup>b)/\text{\AA}</sup>		Edge of octahedron in Fig. 5e ( $r$ )/\text{\AA}		$r_{\text{red}}/r_{\text{blue}}$
						with Y	with apical X of Mo <sub>6</sub> X <sub>14</sub>	$r_{\text{blue}}$	$r_{\text{red}}$	
TSF <b>1</b>	Cl	Cl	10.9080(7)	102.3484(3)	1191.8(1)	3.2082(4)	3.2702(9)	6.839	8.498	1.24
TSF <b>2</b>	Br	Br	11.1579(5)	101.800(1)	1286.3(1)	3.3252(6)	3.3600(8)	7.037	8.659	1.23
TTF <sup>c)</sup>	Cl	Cl	10.685(1)	101.54(1)	1134(4)	3.230(2)	3.260(2)	6.758	8.277	1.23
TTF <sup>c)</sup>	Br	Cl	10.899(1)	100.80(1)	1215(4)	3.312(2)	3.331(2)	6.947	8.398	1.21
TTF <sup>d)</sup>	Br	Br	10.9429(5)	100.915(1)	1228.5(1)	3.352(2)	3.353(2)	6.967	8.439	1.21
TTF <sup>c)</sup>	Br	I	11.033(1)	101.35(1)	1251(6)	3.408(2)	3.409(2)	6.992	8.535	1.22

a) D: donor. b) The sum of van der Waals radii: 3.65 Å for Se–Cl, 3.75 Å for Se–Br, 3.55 Å for S–Cl, and 3.65 Å for S–Br.<sup>[27]</sup> c) Crystallographic data from Ref. 19b. d) Data for newly prepared crystal in our lab, which is in good agreement with the structural analysis in Ref. 19b.



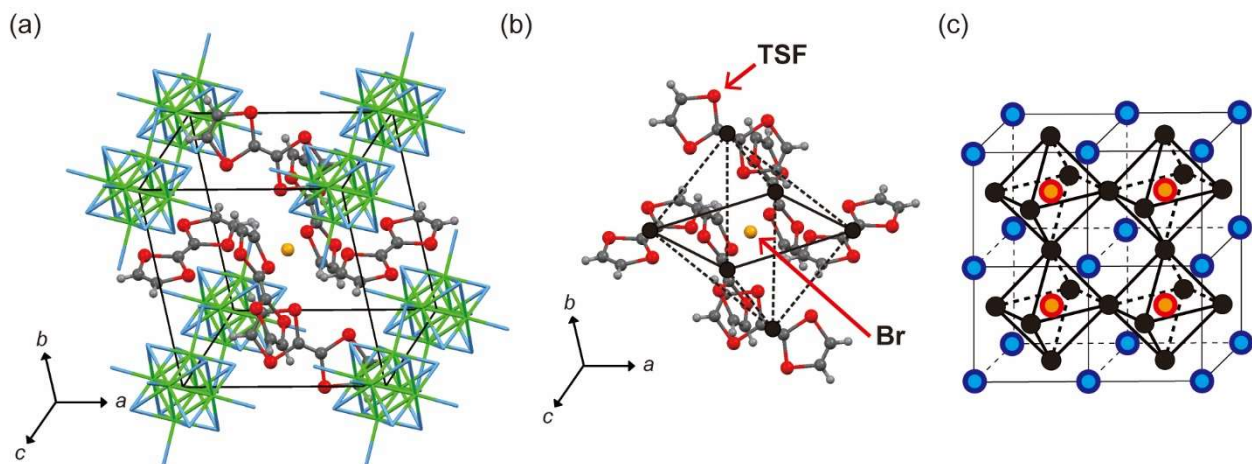


**Fig.4.** (a) Crystal structure of (TSF<sup>+</sup>)<sub>3</sub>[(Mo<sub>6</sub>Br<sub>14</sub>)<sub>2</sub>]<sup>-</sup>Br<sup>-</sup> (**2**) depicted in ball and stick style. TSF molecules and bromine anion are depicted as balls (gray, dark gray, red, and orange balls are hydrogen, carbon, selenium, and bromine atoms, respectively.) [Mo<sub>6</sub>Br<sub>14</sub>] cluster units are depicted as sticks (green and aqua sticks are molybdenum and bromine atoms, respectively). (b) Unit of octahedral lattice with six TSF molecules and Y = Br. The center of TSF is represented by a black circle. Y = Br (orange) is located at the center of the rectangle represented by solid lines. Octahedral lattice of (TSF)<sub>6</sub>Y is made by connecting six black circles (solid and dotted black lines). (c) TSF (or TTF) is represented by black balls, Y by orange balls, and Mo clusters by cyan balls to show a schematic view of the antiperovskite structure.

No structural phase transition was observed in the measured temperature range (300–25 K) for **1** and **2**. Furthermore, Raman spectra of **2** (Fig. S5) in the temperature range from 300–10 K indicate that the charge on the TSF moiety remains unchanged as no significant shift was observed for the charge sensitive bands assigned as  $a_g\nu_2$  and  $a_g\nu_3$  modes (Fig. S2), with the exception of the change in intensity of overtone and combination bands. The molecular charge of the TSF moiety in **2** is estimated to be +1 by comparing the observed modes with calculated ones of TSF<sup>0</sup> and TSF<sup>1+</sup> (Fig. S4, Table S4).

We have studied several CT solids of [Mo<sub>6</sub>X<sub>14</sub>]<sup>n-</sup> and discussed the charge of the donor species based on the Mo–Mo, Mo–X<sup>i</sup>, and Mo–X<sup>a</sup> interatomic distances in combination with other optical methods.<sup>[28]</sup> Some of them are presented in Table 2 together with those of (TBA)<sub>2</sub>[Mo<sub>6</sub>Cl<sub>14</sub>] and Cs<sub>2</sub>[Mo<sub>6</sub>Br<sub>14</sub>].<sup>[20]</sup> Since the molecular structure of neutral and –1 charge species of [Mo<sub>6</sub>X<sub>14</sub>]<sup>n-</sup> are not available, the charge estimated by the bond lengths of [Mo<sub>6</sub>X<sub>14</sub>]<sup>2-</sup> may not be completely accurate. However, the observed distances show excellent consistency with the –2 charge of [Mo<sub>6</sub>X<sub>14</sub>]<sup>n-</sup>. The Raman spectral results as well as the assignment of the charge of Mo cluster units support the +1 charge of the TSF moiety ( $S = 1/2$ ), which is consistent with the SQUID and EPR data (*vide infra*); satisfying requirement [A] for a QSL system.

**Table 2.** Average Mo–Mo, Mo–X<sup>i</sup>, and Mo–X<sup>a</sup> interatomic distances (Å)

Salt of [Mo <sub>6</sub> X <sub>14</sub> ] cluster unit		Mo–Mo	Mo–X <sup>i</sup>	Mo–X <sup>a</sup>	Charge on [Mo <sub>6</sub> X <sub>14</sub> ]	Ref.
Cs <sub>2</sub> [Mo <sub>6</sub> Br <sub>14</sub> ]		2.635	2.601	2.600	–2	20a
(TBA) <sub>2</sub> [Mo <sub>6</sub> Cl <sub>14</sub> ]		2.602	2.469	2.420	–2	20b
Donor of CT solid <sup>a)</sup>		X				
TTT	Br	2.635	2.606	2.594	–2	28a
BO	Br	2.630	2.604	2.594	–2	28a
Perylene	Br	2.637	2.604	2.586	–2	28a
Coronene	Cl	2.607	2.478	2.426	–2	28b
Coronene	Br	2.633	2.599	2.592	–2	28b
TSF <b>1</b>	Cl	2.608	2.476	2.430	–2	This work
TSF <b>2</b>	Br	2.635	2.602	2.594	–2	This work
(TTF) <sub>3</sub> [(Mo <sub>6</sub> Br <sub>14</sub> )Br]		2.635	2.603	2.594	–2	This work

a) TTT: tetrathionaphthalene, BO: bis(ethylenedioxy)-TTT.

**Figure 5** shows the relationship between the spin site (key) and the architecture (keyhole), which holds the key part for  $(\text{TTF or TSF})_3[(\text{Mo}_6\text{X}_{14})\text{Y}]$ . The keyhole is the lattice formed by the  $[\text{Mo}_6\text{X}_{14}]^{2-}$  cluster units (**Figs. 5a and 5a'**), whereas the key is the octahedral spin lattice unit of  $[(\text{TTF or TSF})_6\text{Y}]$  (**Figs. 5b and 5b'**). The cluster units form a pseudocubic arrangement, in which each corner is occupied by a cluster and the spin site  $[(\text{TTF or TSF})_6\text{Y}]$  fits into the center of the cube. Such key(spinner-site)–keyhole(architecture) consideration would provide a clue to develop new spin-frustrated system. The  $(\text{TTF or TSF})_3[(\text{Mo}_6\text{X}_{14})\text{Y}]$  crystal is assembled by nesting the key into the keyhole equivalent to the unit cell through short atomic contacts and Coulomb interactions (**Figs. 5c and c'**). However, the actual structure of the rhombohedral unit cell ( $\alpha \sim 101\text{--}102^\circ$ , **Table 1**) is a distorted octahedron (**Fig. 5d**), resulting in two different distances between the centers of TTF (or TSF) molecules, as depicted in blue and red in **Fig. 5e** and summarized in **Table 1**. It is noticeable that the ratios of the distances in blue and red ( $r_{\text{red}}/r_{\text{blue}}$ ) are nearly identical among the  $(\text{TTF or TSF})_3[(\text{Mo}_6\text{X}_{14})\text{Y}]$  salts, as shown in **Table 1**, since  $r_{\text{red}}/r_{\text{blue}}$  is proportional to angle  $\alpha$  ( $r_{\text{red}}/r_{\text{blue}} = 1$  at  $\alpha = 90^\circ$ ). The difference in the distances and relative orientation between two TTF (or TSF) molecules gives rise to two different overlap integrals,  $s_1$  and  $s_2$  (*vide infra*). This indicates that the  $(\text{TTF or TSF})_3[(\text{Mo}_6\text{X}_{14})\text{Y}]$  salts roughly satisfy requirement **[D]**, but not in the strict sense. The strictness of requirement **[D]** for a QSL system is discussed in Section 3.3.

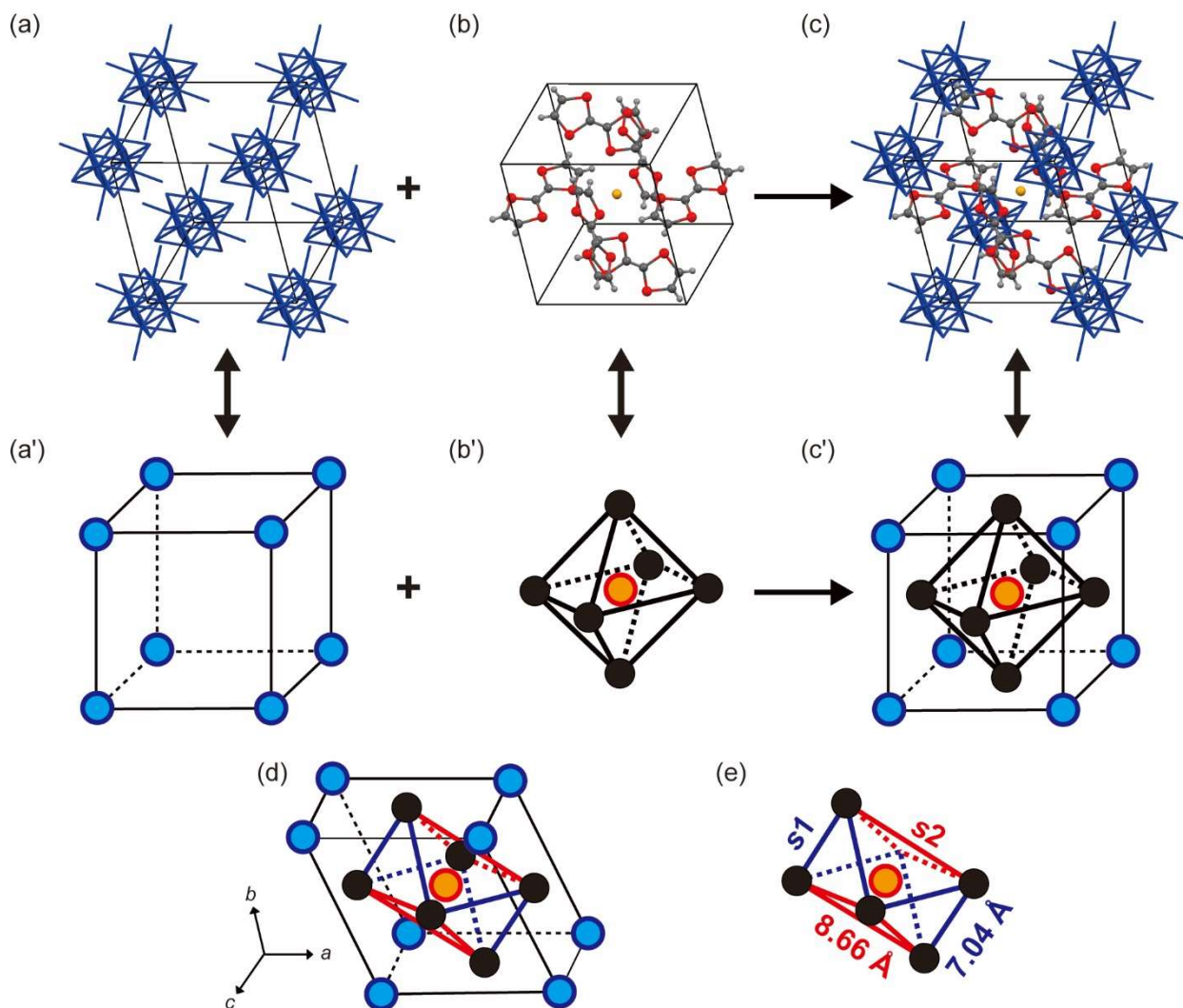


**Fig. 5.** Key-keyhole relationship of  $(\text{TTF or TSF})_3[(\text{Mo}_6\text{X}_{14})\text{Y}]$ . (a, a') The lattice formed by  $[\text{Mo}_6\text{X}_{14}]^{2-}$  cluster units. (b, b') The lattice composed of  $\text{TTF}^{2+}$  (or  $\text{TSF}^{2+}$ ) and  $\text{Y}^-$ . (c, c') Unit cell of  $(\text{TTF or TSF})_3[(\text{Mo}_6\text{X}_{14})\text{Y}]$ . (d) Rhombohedral packing of  $(\text{TTF or TSF})_3[(\text{Mo}_6\text{X}_{14})\text{Y}]$ . Blue circles:  $[\text{Mo}_6\text{X}_{14}]^{2-}$  cluster units. Orange circle:  $\text{Y}^-$ . Black circles:  $\text{TTF}^{2+}$  or  $\text{TSF}^{2+}$ . (e) Overlap integrals  $s_1$ (blue) and  $s_2$ (red) between TTF (or TSF) molecules in  $(\text{TTF or TSF})_3[(\text{Mo}_6\text{X}_{14})\text{Y}]$ . The intersite distances are those of  $(\text{TSF})_3[(\text{Mo}_6\text{Br}_{14})\text{Br}]$ .

### 3.2. Transport and magnetic properties

Both TSF salts **1** and **2** are semiconducting with RT resistivities ( $\rho_{\text{RT}}$ ) of  $3 \times 10^4 \Omega\text{cm}$  (activation energy ( $\varepsilon_a$ ) = 0.12 eV) and  $2 \times 10^4 \Omega\text{cm}$  ( $\varepsilon_a$  = 0.08 eV), respectively (Fig. S6). The temperature dependence of static magnetic susceptibility ( $\chi$ ),  $\chi$  behavior in various magnetic fields, and magnetic field dependence of  $dM/dH$  of **2** are shown in Fig. 6, with **1** exhibiting similar behavior (Fig. S7). The  $\chi$  at RT ( $\chi_{\text{RT}}$ ) is  $1.23 \times 10^{-3} \text{ emu spin}^{-1}$  for **1** and  $1.12 \times 10^{-3} \text{ emu spin}^{-1}$  for **2**, both of which are larger than that of  $(\text{TTF})_3[(\text{Mo}_6\text{Br}_{14})\text{Br}]$  ( $1.06 \times 10^{-3} \text{ emu spin}^{-1}$ ) (Fig. S8(a)). These  $\chi_{\text{RT}}$  values are the same as those of typical ET Mott insulators, where  $\chi_{\text{RT}}$  is  $9\text{--}12 \times 10^{-4} \text{ emu mol}^{-1}$ .<sup>[16]</sup> From RT to 20 K, these values obey the Curie–Weiss law with a Curie constant ( $C$ ) of  $0.370 \text{ emu K spin}^{-1}$  and  $\Theta_{\text{CW}}$  of  $-1.6 \text{ K}$  for **1** and  $C = 0.342 \text{ emu K spin}^{-1}$  and  $\Theta_{\text{CW}} = -6.3 \text{ K}$  for **2**, indicating considerably weaker AF interactions than those in TTF salts<sup>[19]</sup> ( $\Theta_{\text{CW}}$ :  $-14.6 \sim -11.5 \text{ K}$ ). In the lowest temperature region,  $\chi$  undergoes a sharp decrease at 3.0 K for **1** and 5.5 K for **2**, as seen in Figs. 6(a) and S7(a), which could be suppressed by applying a magnetic field (insets of Figs. 6(a) and S7(a)). This confirms that the ground state of these solids are the Néel state and the occurrence of the spin-flop transition at high magnetic fields. The  $T_{\text{N}}$  is lower than those observed for TTF analogs (Table 3). For the spin-flop field ( $H_{\text{sf}}$ ), Fig. 6b clearly shows a peak corresponding to the  $H_{\text{sf}}$  at 1.5 T (3.2 T for **1** in Fig. S7(b)). Although  $H_{\text{sf}}$  was not explicitly determined,  $(\text{TTF})_3[(\text{Mo}_6\text{Br}_{14})\text{Br}]$  also exhibits the spin-flop phenomenon between 0.1 and 0.2 T at 1.9 K (Figs. S8(a) and (b)). Table 3 summarizes the transport and magnetic properties of  $(\text{TTF or TSF})_3[(\text{Mo}_6\text{X}_{14})\text{Y}]$ . These results, together with the structural analyses and estimated charge on the TSF species, confirm that these salts are Mott insulators and satisfy requirement [B] for a QSL system.

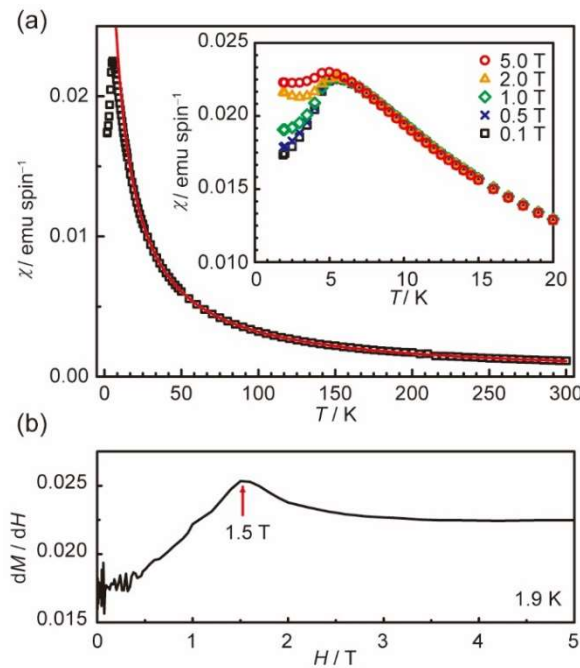




**Fig. 6.** (a) Temperature dependence of static magnetic susceptibility of polycrystalline **2** at 0.1 T. Solid red line is the Curie–Weiss fit with  $C = 0.342 \text{ emu K spin}^{-1}$  and  $\Theta_{\text{CW}} = -6.3 \text{ K}$ . Inset shows the magnetic field dependence (0.1–5.0 T) of  $\chi$  below 20 K. (b)  $dM/dH$  as a function of magnetic field at 1.9 K. A scatter of  $dM_p/dH$  at the region of  $H = 0.1\text{--}0.45 \text{ T}$  resulted from inherent properties of the superconducting magnet. A red arrow indicates the spin-flop magnetic field.

**Table 3** Transport and magnetic properties and calculated overlap integrals of  $(\text{TTF or TSF})_3[(\text{Mo}_6\text{X}_{14})\text{Y}]$

$\text{D}^{++}$	X in $[\text{Mo}_6\text{X}_{14}]^{2-}$	$\text{Y}^-$	$\Theta_{\text{CW}} / \text{K}$	$T_{\text{max}}^{\text{a)}}$ / K	$T_{\text{N}}^{\text{b)}}$ / K	Ref.	$f$	$\chi_{\text{RT}} / \text{emu mol}^{-1}$	$H_{\text{sf}} / \text{T}$	$\rho_{\text{RT}} / \Omega \text{cm}$	$s^1 / 10^{-3}$	$s^2 / 10^{-4}$	$ s^2 / s^1 $	Ref.
TSF	<b>1</b> Cl	Cl	-1.6	3.0	3.0	This work	0.53	$1.23 \times 10^{-3}$	3.2	$3 \times 10^4$	3.61	7.01	0.20	This work
	<b>2</b> Br	Br	-6.3	5.5	5.5	This work	1.15	$1.12 \times 10^{-3}$	1.5	$2 \times 10^4$	3.48	3.56	0.10	This work
TTF	Cl	Cl	-14.6	11	8.2	19b	1.78	—	—	—	1.12	-0.93	0.08	This work
	Br	Cl	-16.7	13	8.2	19b	2.04	—	—	—	1.10	-1.75	0.16	This work
	Br	Br	-11.5	11	7.5	19b	1.53	$1.06 \times 10^{-3}$	0.1~0.2	—	1.05	-1.21	0.11	This work
	Br	I	-12.1	8	6.2	19b	1.95	—	—	—	0.86	-0.76	0.09	This work

a)  $T_{\text{max}}$ : peak temperature of  $\chi$  in SQUID measurement. b)  $T_{\text{N}}$  was evaluated by EPR measurement in [ref. 19](#). For **1** and **2**,  $T_{\text{max}}$  was used as  $T_{\text{N}}$ , as  $T_{\text{N}}$  could not be evaluated by EPR measurement.

**Figure 7** presents the EPR data of **2**. The  $g$ -factor at RT was 2.0301, which is in agreement with the  $\text{TSF}^{++}$  species ( $S = 1/2$ ) ( $g_{\text{AV}} = 2.027$ ).<sup>[29]</sup> The EPR linewidth ( $\Delta H$ ) and  $g$ -factor show an increase below *ca.* 45 K that may be ascribed to the low-dimensional fluctuation of AF ordering. Below 5 K, both EPR parameters increase rapidly, owing to the 3D AF ordering.

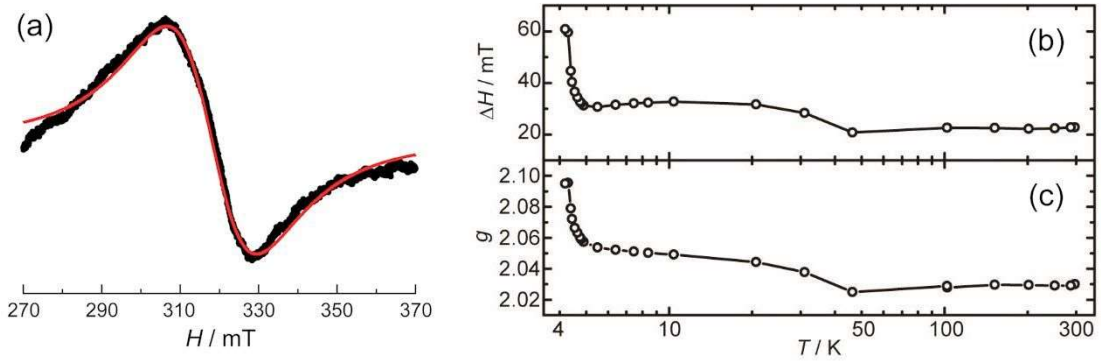


**Fig. 7.** (a) EPR spectrum of a single crystal of **2** at RT, where a red line shows a single Lorentzian line centered at  $g = 2.0301$ . Temperature dependence of (b) EPR linewidth ( $\Delta H$ ) and (c)  $g$ -value.

To give microscopic insight into the ground state, the  $^1\text{H}$  NMR spectrum was measured for a randomly orientated polycrystalline sample of **2**. The temperature dependence of the  $^1\text{H}$  NMR spectra in [Fig. 8a](#) shows broadening and splitting upon cooling, as indicated by blue and red arrows for the higher and lower frequency peaks, respectively. At high temperatures, the spectral shape is dominated by  $^1\text{H}\text{--}^1\text{H}$  nuclear dipole coupling. As the spin susceptibility increases, anisotropic hyperfine and dipole fields from electron spins become visible at the  $^1\text{H}$  sites, giving an anisotropic powder pattern to the NMR spectra. In [Fig. 8b](#), we plot the Knight shifts defined as peak frequencies measured from the central frequency at high temperatures. The Knight shift for a low-frequency peak well correlates to the spin susceptibility as an implicit function of temperature, as shown in [Fig. 8c](#), which yields a hyperfine coupling constant of  $-0.15 \text{ kOe } \mu_{\text{B}}^{-1}$ . The Knight shift for a high-frequency peak behaves nearly independent of temperature because of the vanishing hyperfine coupling. A prominent spectral broadening occurs below 5 K, clearly indicating the magnetic order. Using the hyperfine coupling, the observed local field of 1 MHz at 4.2 K corresponds to a

magnetic moment of  $1.1\mu_B$ , as shown in Fig. 8d. The  $^1\text{H}$  NMR spin-lattice relaxation rate ( $T_1^{-1}$ ) shows a divergent peak around 5 K, indicating the 3D nature of the AF transition (Fig. 8e).

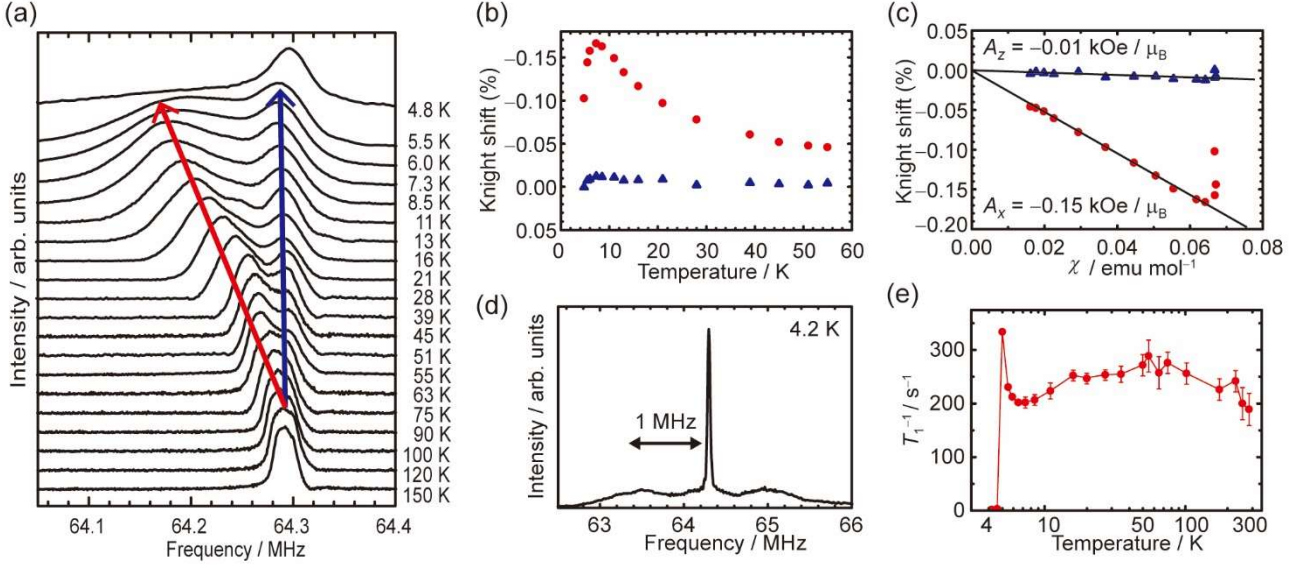


**Fig. 8.**  $^1\text{H}$  NMR spectra of polycrystalline **2**. Temperature dependence of (a)  $^1\text{H}$  NMR spectra; high- and low-frequency peaks are indicated by blue and red arrows, respectively. (b) Temperature dependence of Knight shift. (c) The Knight shifts vs. magnetic susceptibility, where the linearity gives the principal components of the hyperfine coupling,  $A_z = -0.01$  and  $A_x = -0.15$  kOe  $\mu_B^{-1}$ . In (b) and (c), blue and red symbols correspond to the blue and red arrows in (a), respectively. (d) The spectrum in the magnetically ordered state at 4.2 K. The sharp central peak comes from the H sites with negligible hyperfine coupling constants. (e) Temperature dependence of nuclear spin-lattice relaxation rate ( $T_1^{-1}$ ).

### 3.3. Geometry of spin lattice and spin frustration

Table 3 also summarizes the overlap integrals of  $(\text{TTF or TSF})_3[(\text{Mo}_6\text{X}_{14})\text{Y}]$ . The absolute  $s1$  values for the TSF salts ( $3.5\text{--}3.6 \times 10^{-3}$ ) lie within those of interdimer overlap integrals observed for the  $\kappa\text{-(ET)}_2\text{X}$  salts ( $2.9\text{--}11.5 \times 10^{-3}$ ), which cover Mott insulators, AFs, QSLs, metals, and superconductors.<sup>[30]</sup> Consequently, as long as  $s1$  concerns, the TSF salts may reside near the Mott boundary if the  $U$  values are comparable to those of dimer-type conductors,  $\kappa\text{-(ET)}_2\text{X}$  ( $U_d = 0.45\text{--}0.51$  eV<sup>[16]</sup> by extended Hückel method, where  $U_d$  is the Coulomb repulsive energy between two electrons on a dimer). However, monomer-type systems such as the present salts have much larger  $U$  values than  $U_d$  for  $\kappa\text{-(ET)}_2\text{X}$ , as two electrons are present on one molecule.

In the monomer-type systems, the  $U$  value is approximated as  $(U_0 - V)$ , where  $U_0$  is bare on-site Coulomb repulsion and  $V$  is neighboring-site Coulomb repulsion (Fig. 9). We estimated the  $U$  values of **1**, **2**, and  $(\text{TTF})_3[(\text{Mo}_6\text{Br}_{14})\text{Br}]$  through observation of the first CT absorption band peak.<sup>[31]</sup> The present salts do not possess such regular segregated columns as depicted in Fig. 9, and the distance between neighboring sites is larger compared to the conventional 1D segregated column. Hence, the absorption band originating from  $U$  for these salts is not well separated from the higher energy bands and appeared as a shoulder (Fig. S9). The  $U$  values derived from the absorption peaks were estimated as 1.2–1.4 eV for **1** and **2** and 1.4–1.5 eV for  $(\text{TTF})_3[(\text{Mo}_6\text{Br}_{14})\text{Br}]$ . Accordingly, the transfer interactions derived from overlap integral  $s1$  are much smaller compared to the effective  $U$  value for  $(\text{TSF})_3[(\text{Mo}_6\text{X}_{14})\text{Y}]$ , indicating that the localized spin

nature is in good accordance with the transport results. The  $s1$  values of TTF salts are about three times smaller ( $0.86\text{--}1.1 \times 10^{-3}$ ) than those of TSF salts, suggesting a more localized nature of the TTF salts.

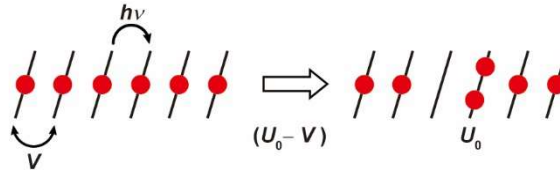


**Fig. 9.** One-electron transfer in a Mott insulator (thick bars and red balls represent molecules and radical electrons, respectively) costs energy of effective  $U$  ( $= U_0 - V$ ) approximately. Such electron transfer is observed as the first absorption band in optical measurements of fully ionized radical CT salts.

The edges drawn by blue lines ( $s1$ ) in **Fig. 5e** possess one order of magnitude larger overlap integrals than the red lines ( $s2$ ) of the octahedron ( $|s1| > |s2|$ ), mainly owing to the shorter distance (7.04 Å for  $s1$  vs. 8.66 Å for  $s2$  in **2**). Furthermore, the anisotropic molecular orbital of organic molecules causes a larger difference in  $s1$  and  $s2$  by forming different relative orientations between two TTF (or TSF) molecules (**Fig. 10a** for  $s1$  and **Fig. 10b** for  $s2$ ). The very small  $s2$  values for both antiperovskite systems ( $3.6\text{--}7.0 \times 10^{-4}$  for TSF salts and  $0.76\text{--}1.8 \times 10^{-4}$  for TTF salts) cause them to be 3D Mott insulators.

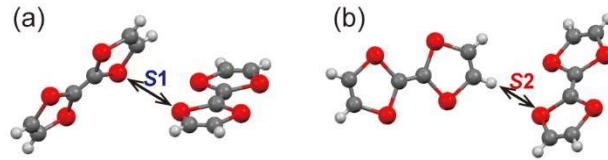


**Fig. 10.** Relative orientations of two TTF (or TSF) molecules for overlap integrals (a)  $s1$  and (b)  $s2$ .

**Table 3** includes the ratio  $|s2|/|s1|$ , which corresponds to  $t'/t$  in the case of a 2D isosceles triangle lattice, a parameter for the spin frustration concerning the triangle composed of two blue edges and one red edge. The ratio  $|s2|/|s1|$  is much smaller than unity, indicating that the spin frustration is not significant.

Since the spin frustration is enhanced when  $|s2|/|s1|$  approaches unity, it may be reasonable that the  $T_N$  values of TSF salts (3.0 K for **1**, 5.5 K for **2**) are lower than those observed for TTF salts in accordance with increased  $|s2|/|s1|$ . The increase of  $|s2|/|s1|$  to unity is favorable for the QSL state; however, upon decreasing temperature, the  $|s2|/|s1|$  values decrease to 0.18 and 0.10 at 100 K and 0.17 and 0.09 at 25 K for **1** and **2**, respectively.

The antiperovskite system  $(\text{TTF or TSF})_3[(\text{Mo}_6\text{X}_{14})\text{Y}]$  was found to have weak spin frustration in terms of  $f$  (**Table 3**). Since the  $J$  value is represented by **Eq. 1** and  $U$  of the TSF molecule is smaller than that of the TTF molecule, the  $|\mathcal{O}_{\text{CW}}|$  values of the TSF salts are thought to be larger than those of the TTF salts. However, the experimental results are the opposite of this expectation in that the  $|\mathcal{O}_{\text{CW}}|$  values of the TSF salts are smaller than those of the TTF salts, even though the absolute values of  $s1$  and  $s2$  are three times larger than those of TTF salts. The reason for this discrepancy is currently unknown. The AF interactions represented by  $\mathcal{O}_{\text{CW}}$  are very weak in this antiperovskite system, compared with the QSL systems:  $|\mathcal{O}_{\text{CW}}| = 300, 325\text{--}375, 375, \text{ and } 650$  K for  $\text{ZnCu}_3(\text{OH})_6\text{Cl}_2$ ,  $\text{EtMe}_3\text{Sb}[\text{Pd}(\text{dmit})_2]_2$ ,  $\kappa\text{-(ET)}_2\text{Cu}_2(\text{CN})_3$ , and  $\text{Na}_4\text{Ir}_3\text{O}_8$ , respectively.<sup>[7,11,13,14]</sup> As such, the distorted octahedral spin lattice of  $(\text{TTF or TSF})_3[(\text{Mo}_6\text{X}_{14})\text{Y}]$  is not a QSL system candidate.

Although the antiperovskite salts  $(\text{TTF or TSF})_3[(\text{Mo}_6\text{X}_{14})\text{Y}]$  satisfy requirements [A] and [B] for a QSL system, they do not satisfy requirements [D] and [E], ruling out the possibility of a QSL state and allowing for the AF Néel state with low  $|\mathcal{O}_{\text{CW}}|$  and  $T_{\text{N}}$ . Thus, an undistorted octahedral  $[(\text{donor}^{*+})_6\text{Y}^-]$  unit composed of donor molecules having small effective  $U$  values with equal and large overlap integrals between spin sites will be envisaged.

#### 4. Conclusion

TSF molecules afforded antiperovskite salts,  $(\text{TSF})_3[(\text{Mo}_6\text{X}_{14})\text{Y}]$  ( $\text{X} = \text{Y} = \text{Cl}$ : **1** and  $\text{X} = \text{Y} = \text{Br}$ : **2**), isostructural to the TTF analogs. Their crystal structures are interpreted by a key–keyhole relationship between distorted octahedral spin sites  $[(\text{TTF or TSF})_6\text{Y}]$  and the rhombohedral lattice, the corners of which are occupied by cluster anions  $[\text{Mo}_6\text{X}_{14}]^{n-}$ . The bond lengths of  $[\text{Mo}_6\text{X}_{14}]^{n-}$  determined by structural analysis suggest that it is in a dianionic state,  $[\text{Mo}_6\text{X}_{14}]^{2-}$ , which results in a +1 charge of the TSF species ( $S = 1/2$ ). This valence of TSF was confirmed by Raman and EPR measurements. The crystal structure and semiconductive nature indicate that they are 3D Mott insulators at RT. A 3D AF ordering occurs and the  $T_{\text{N}}$  temperatures for the TSF solids ( $T_{\text{N}} = 3.0$  K for **1** and 5.5 K for **2**) are lower than those for the TTF solids, owing to higher spin frustration in terms of  $|s_2|/|s_1|$ . Spin-flop was detected for TSF salts at 3.2 T for **1** and 1.5 T for **2** at 1.9 K. Such spin-flop was also detected for  $(\text{TTF})_3[(\text{Mo}_6\text{Br}_{14})\text{Br}]$  at 0.1–0.2 T at 1.9 K. Although the salts satisfy requirements [A] and [B] for a QSL system, they do not satisfy requirements [D] and [E]. Owing to both the distortion of the octahedral geometry of the spin lattice and the anisotropic molecular orientation, the geometrical spin frustration in both TSF and TTF systems is weakened. In order to have strong geometrical spin frustration toward the QSL state,  $|s_1| \sim |s_2|$  and larger  $s$  values are essential.

#### Acknowledgments.

The work was supported by JSPS KAKENHI Grants (23225005 and 26288035). Thanks are due to the Instrument Center, the Institute for Molecular Science, for assistance in obtaining the single crystal diffraction data at 25 K.

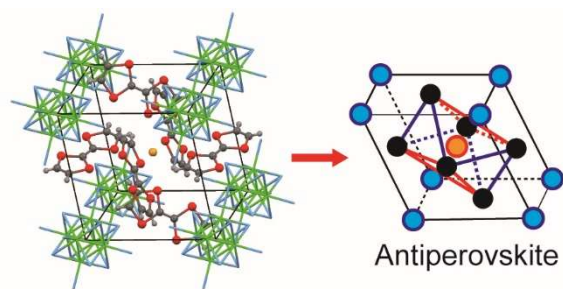
#### References

1. a) P. W. Anderson, *Mater. Res. Bull.*, 1973, **8**, 153-160.  
b) P. Fazekas, P. W. Anderson, *Philos. Mag.*, 1974, **30**, 423-440.
2. G. H. Wannier, *Phys. Rev.* 1950, **79**, 357-364.
3. a) A. P. Ramirez, *Annul. Rev. Mater. Sci.*, 1994, **24**, 453-480.  
b) J. E. Greedan, *J. Mater. Chem.*, 2001, **11**, 37-53.
4. a) D. A. Huse, V. Elser, *Phys. Rev. Lett.*, 1988, **60**, 2531-2534.  
b) L. F. Tocchio, C. Gros, R. Valenti, F. Becca, *Phys. Rev. B*, 2014, **89**, 235107/1-9.  
c) A. Yamada, *Phys. Rev. B*, 2014, **89**, 195108/1-9.
5. P. Schiffer, A. P. Ramirez, *Comments Condens. Matter Phys.*, 1996, **18**, 21-50.
6. a) K. Hirakawa, H. Kadowaki, K. Ubukoshi, *J. Phys. Soc. Jpn.*, 1983, **52**, 1814-1824.  
b) J. L. Manson, E. Ressouche, J. S. Miller, *Inorg. Chem.*, 2000, **39**, 1135-1141.
7. a) Y. Shimizu, K. Miyagawa, K. Kanoda, M. Maesato, G. Saito, *Phys. Rev. Lett.*, 2003, **91**, 107001/1-4.  
b) S. Ohira, Y. Shimizu, K. Kanoda, G. Saito, *J. Low Temp. Phys.*, 2006, **142**, 153-158.  
c) Y. Shimizu, H. Kasahara, T. Furuta, K. Miyagawa, K. Kanoda, M. Maesato, G. Saito, *Phys. Rev. B*, 2010, **81**, 224508/1-4.  
d) F. L. Pratt, P. J. Baker, S. J. Blundell, T. Lancaster, S. Ohira-Kawamura, C. Baines, Y. Shimizu, K. Kanoda, I. Watanabe, G. Saito, *Nature*, 2011, **471**, 612-616.

- e) Y. Shimizu, M. Maesato, G. Saito, *J. Phys. Soc. Jpn.*, 2011, **80**, 074702/1-7.
8. L. Balents, *Nature*, 2010, **464**, 199-208.
9. M. R. Norman, *Science*, 2011, **332**, 196-200.
10. B. J. Powell, R. H. McKenzie, *Rep. Prog. Phys.* 2011, **74**, 056501/1-60.
11. T. Itou, A. Oyamada, S. Maegawa, M. Tamura, R. Kato, *J. Phys.: Condens. Matter*, 2007, **19**, 145247/1-5.
12. T. Isono, H. Kamo, A. Ueda, K. Takahashi, M. Kimata, H. Tajima, S. Tsuchiya, T. Terashima, S. Uji, H. Mori, *Phys. Rev. Lett.*, 2014, **112**, 177201/1-5.
13. a) T.-H. Han, J. S. Helton, S. Chu, D. G. Nocera, J. A. Rodriguez-Rivera, C. Broholm, Y. S. Lee, *Nature*, 2012, **492**, 406-410.  
b) J. S. Helton, K. Matan, M. P. Shores, E. A. Nytko, B. M. Bartlett, Y. Yoshida, Y. Takano, A. Suslov, Y. Qiu, J.-H. Chung, D. G. Nocera, Y. S. Lee, *Phys. Rev. Lett.*, 2007, **98**, 107204/1-4.
14. a) Y. Okamoto, M. Nohara, H. Aruga-Katori, H. Takagi, *Phys. Rev. Lett.*, 2007, **99**, 137207/1-4.  
b) R. R. P. Singh, J. Oitmaa, *Phys. Rev. B*, 2012, **85**, 104406/1-4.
15. Y. Yoshida, H. Ito, M. Maesato, Y. Shimizu, H. Hayama, T. Hiramatsu, Y. Nakamura, H. Kishida, T. Koretsune, C. Hotta, G. Saito, *Nat. Phys.*, 2015, **11**, 679-683.
16. T. Hiramatsu, Y. Yoshida, G. Saito, A. Otsuka, H. Yamochi, M. Maesato, Y. Shimizu, H. Ito, H. Kishida, *J. Mater. Chem. C*, 2015, 1378-1388. Even though the following solid is reported as a QSL candidate with  $S = 1$  ( $\text{Ba}_3\text{NiSb}_2\text{O}_9$ , J. G. Cheng, G. Li, L. Balicas, J. S. Zhou, J. B. Goodenough, C. Xu, H. D. Zhou, *Phys. Rev. Lett.*, 2011, **107**, 197204/1-4), considering its small  $|\Theta_{\text{CW}}|$  ( $= 75.6$  K), and  $f(> 216)$  values, the solid should be studied down to much lower temperatures in order to confirm its QSL state.
17. C. Livage, N. Guillou, J. Chaigneau, P. Rabu, M. Drillon, G. Ferey, *Angew. Chem. Int. Ed.* 2005, **44**, 6488-6491.
18. K. Takenaka, *Sci. Technol. Adv. Mater.* 2012, **13** 013001/1-11.
19. a) P. Batail, L. Ouahab, A. Penicaud, C. Lenoir, A. Perrin, *C. R. Acad. Sc. Paris, série II*, 1987, **304 n°18**, 1111-1116. It was shown later that the actual compound contained a mixture of monoanionic and dianionic cluster units (see ref. [19b](#)).  
b) P. Batail, C. Livage, S. S. P. Parkin, C. Coulon, J. D. Martin, E. Canadell, *Angew. Chem. Int. Ed.*, 1991, **30**, 1498-1500.
20. a) K. Kirakci, S. Cordier, C. Perrin, *Z. Anorg. Allg. Chem.* 2005, **631**, 411-416.  
b) W. Preetz, K. Harder, H. G. von Schnering, G. Kliche, K. Peters, *J. Alloys. Compd.*, 1992, **183**, 413-429.
21. G. M. Sheldrick, *Acta Cryst.* 2008, **A 64**, 112-122.
22. J. C. Scott, S. Etemad, E. M. Engler, *Phys. Rev. B*, 1978, **17**, 2269-2275.
23. A. W. Maverick, J. S. Najdzionek, D. MacKenzie, D. G. Nocera, H. B. Gray, *J. Am. Chem. Soc.*, 1983, **105**, 1878-1882.
24. H. Hosoda, Master thesis Kyoto University (2006).
25. T. Mori, A. Kobayashi, Y. Sasaki, H. Kobayashi, G. Saito, H. Inokuchi, *Bull. Chem. Soc. Jpn.*, 1984, **57**, 627-633.
26. H. Kobayashi, H. Tomita, T. Naito, A. Kobayashi, F. Sakai, T. Watanabe, P. Cassoux, *J. Am. Chem. Soc.* 1996, **118**, 368-377.
27. A. Bondi, *J. Phys. Chem.*, 1964, **68**, 441-451.
28. a) G. Saito, H. Hosoda, Y. Yoshida, J. Hagiwara, K. Nishimura, H. Yamochi, A. Otsuka, T. Hiramatsu, Y. Shimazaki, K. Kirakci, S. Cordier, C. Perrin, *J. Mater. Chem.*, 2012, **22**, 19774-19791.  
b) Y. Yoshida, M. Maesato, Y. Kumagai, M. Mizuno, K. Isomura, H. Kishida, M. Izumi, Y. Kubozono, A. Otsuka, H. Yamochi, G. Saito, K. Kirakci, S. Cordier, C. Perrin, *Eur. J. Inorg. Chem.* 2014, **24**, 3871-3878.
29. a) J. C. Scott, *Mol. Cryst. Liq. Cryst.*, 1982, **79**, 49-59.  
b) W. M. Walsh, L. W. Rupp, F. Wudl, M. L. Kaplan, D. E. Schafer, G. A. Thomas, R. Gemmer, *Solid State Commun.*, 1980, **33**, 413-416.
30. T. Komatsu, N. Matsukawa, T. Inoue, G. Saito, *J. Phys. Soc. Jpn.*, 1996, **65**, 1340-1354.
31. J. B. Torrance, B. A. Scott, B. Welber, F. B. Kaufman, P. E. Seidenm, *Phys. Rev. B*, 1979, **19**, 730-741.



## Table of contents



We report two novel antiperovskite charge-transfer solids,  $(\text{TSF})_3[(\text{Mo}_6\text{X}_{14})\text{X}]$  ( $\text{X} = \text{Cl}, \text{Br}$ ), and discuss spin frustration of their octahedral spin lattices.

## Supporting Information

# Spin Frustration in Antiperovskite Systems: $(\text{TTF}^{\bullet+}$ or $\text{TSF}^{\bullet+})_3[(\text{Mo}_6\text{X}_{14})^{2-}\text{Y}^-]$

Takaaki Hiramatsu,<sup>\*a</sup> Yukihiro Yoshida,<sup>a</sup> Gunzi Saito,<sup>\*a,b</sup> Akihiro Otsuka,<sup>c</sup> Hideki Yamochi,<sup>c</sup> Yasuhiro Shimizu,<sup>d</sup> Yuma Hattori,<sup>e</sup> Yuto Nakamura,<sup>e</sup> Hideo Kishida,<sup>e</sup> Hiroshi Ito,<sup>e</sup> Kaplan Kirakci,<sup>f,‡</sup> Stéphane Cordier,<sup>f</sup> and Christiane Perrin<sup>f</sup>

<sup>a</sup> Faculty of Agriculture, Meijo University, 1-501 Shiogamaguchi, Tempaku-ku, Nagoya 468-8502, Japan

<sup>b</sup> Toyota Physical and Chemical Research Institute, 41-1, Yokomichi, Nagakute, Aichi 480-1192, Japan

<sup>c</sup> Research Center for Low Temperature and Materials Sciences, Kyoto University, Sakyo-ku, Kyoto 606-8501, Japan

<sup>d</sup> Department of Physics, Graduate School of Science, Nagoya University, Chikusa-ku Nagoya 464-8602, Japan

<sup>e</sup> Department of Applied Physics, Nagoya University, Chikusa-ku, Nagoya 464-8603, Japan

<sup>f</sup> Institut des Sciences Chimiques de Rennes, UMR CNRS 6226, Université de Rennes 1, Avenue du Général Leclerc, 35042 Rennes cedex, France

---

Present address ‡ Institute of Inorganic Chemistry of the Academy of Sciences of the Czech Republic

Corresponding authors Takaaki Hiramatsu; E-mail: htakaaki@meijo-u.ac.jp

Gunzi Saito; E-mail: gsaito@meijo-u.ac.jp

**Table S1.** Crystal data and structure refinement of **1**

	<b>1</b>		
Chemical formula	$\text{C}_{18}\text{H}_{12}\text{Cl}_{15}\text{Mo}_6\text{Se}_{12}$		
Molecular weight	2283.19		
Temperature / K	300	100	25
Crystal dimensions / $\text{mm}^3$	$0.17 \times 0.15 \times 0.08$	$0.17 \times 0.15 \times 0.08$	$0.12 \times 0.10 \times 0.06$
Crystal system	Rhombohedral	Rhombohedral	Rhombohedral <sup>†</sup>
Space group	$R\bar{3}$	$R\bar{3}$	$R\bar{3}$ <sup>†</sup>
$a$ / Å	10.9080(7)	10.8505(5)	10.8471(9) <sup>†</sup>
$\alpha$ / °	102.3484(3)	102.6318(2)	102.732(6) <sup>†</sup>
$V$ / Å <sup>3</sup>	1191.8(1)	1167.76(9)	1164.7(5) <sup>†</sup>
$Z$	1	1	1 <sup>†</sup>
$D_{\text{calc}}$ / $\text{g cm}^{-3}$	3.181	3.247	3.255
Diffractionmeter	Bruker APEXII CCD area detector	Bruker APEXII CCD area detector	Rigaku Mercury CCD
Radiation type	MoK $\alpha$	MoK $\alpha$	MoK $\alpha$
Absorption correction	Numerical	Numerical	Numerical
$\mu$ / $\text{mm}^{-1}$	11.554	11.792	11.823
No. of reflections measured	6674	6491	12352
No. of independent reflections	1797	1762	1779
$R_{\text{int}}$	0.0163	0.0143	0.0497
No. of parameters	78	78	78
Final $R_1$ values ( $I > 2\sigma(I)$ )	0.0180	0.0132	0.0151
Final $wR(F^2)$ values ( $I > 2\sigma(I)$ )	0.0343	0.0295	0.0325
Final $R_I$ values (all data)	0.0239	0.0145	0.0168
Final $wR(F^2)$ values (all data)	0.0363	0.0299	0.0325
Goodness of fit of $F^2$	1.094	1.086	1.043
Largest diff. peak / $\text{eÅ}^{-3}$	0.566	0.563	0.811
Largest diff. hole / $\text{eÅ}^{-3}$	−0.477	−0.419	−0.641
CCDC number	999368	999367	999366

(<sup>†</sup>) The values were evaluated by transformation from the hexagonal setting to rhombohedral setting, as data processing and structure analyses were conducted with the hexagonal setting.

**Table S2.** Crystal data and structure refinement of **2**

	<b>2</b>		
Chemical formula	$\text{C}_{18}\text{H}_{12}\text{Br}_{15}\text{Mo}_6\text{Se}_{12}$		
Molecular weight	2950.09		
Temperature / K	298	100	25
Crystal dimensions / $\text{mm}^3$	$0.13 \times 0.10 \times 0.05$	$0.13 \times 0.10 \times 0.05$	$0.13 \times 0.10 \times 0.05$
Crystal system	Rhombohedral	Rhombohedral	Rhombohedral <sup>†</sup>
Space group	$R\bar{3}$	$R\bar{3}$	$R\bar{3}$ <sup>†</sup>
$a$ / Å	11.1579(5)	11.0988(9)	11.090(1) <sup>†</sup>
$\alpha$ / °	101.800(1)	102.0577(4)	102.147(8) <sup>†</sup>
$V$ / Å <sup>3</sup>	1286.3(1)	1261.1(2)	1259.7(7) <sup>†</sup>
$Z$	1	1	1 <sup>†</sup>
$D_{\text{calc}}$ / $\text{g cm}^{-3}$	3.808	3.884	3.889
Diffractionmeter	Bruker APEXII CCD area detector	Bruker APEXII CCD area detector	Rigaku Mercury CCD
Radiation type	MoK $\alpha$	MoK $\alpha$	MoK $\alpha$
Absorption correction	Numerical	Numerical	Numerical
$\mu$ / $\text{mm}^{-1}$	21.576	22.007	22.032
No. of reflections measured	7248	7072	13558
No. of independent reflections	1939	1903	1931
$R_{\text{int}}$	0.0228	0.0195	0.0541
No. of parameters	78	78	78
Final $R_1$ values ( $I > 2\sigma(I)$ )	0.0252	0.0203	0.0322
Final $wR(F^2)$ values ( $I > 2\sigma(I)$ )	0.0454	0.0395	0.0669
Final $R_I$ values (all data)	0.0382	0.0258	0.0354
Final $wR(F^2)$ values (all data)	0.0488	0.0409	0.0691
Goodness of fit of $F^2$	1.026	1.013	1.130
Largest diff. peak / $\text{eÅ}^{-3}$	0.582	0.536	1.530
Largest diff. hole / $\text{eÅ}^{-3}$	−0.426	−0.491	−1.201
CCDC number	999365	999364	999363

(<sup>†</sup>) The values were evaluated by transformation from the hexagonal setting to rhombohedral setting, as data processing and structure analyses were conducted with the hexagonal setting.

**Table S3.** Crystal data and structure refinement of (TTF)<sub>3</sub>[(Mo<sub>6</sub>Br<sub>14</sub>)Br]

	(TTF) <sub>3</sub> [(Mo <sub>6</sub> Br <sub>14</sub> )Br]	
Chemical formula	C <sub>18</sub> H <sub>12</sub> Br <sub>15</sub> Mo <sub>6</sub> S <sub>12</sub>	
Molecular weight	2387.29	
Temperature / K	300	100
Crystal dimensions / mm <sup>3</sup>	0.18 × 0.16 × 0.11	0.18 × 0.16 × 0.11
Crystal system	Rhombohedral	Rhombohedral
Space group	$R\bar{3}$	$R\bar{3}$
$a$ / Å	10.9429(5)	10.8797(5)
$\alpha$ / °	100.915(1)	101.159(1)
$V$ / Å <sup>3</sup>	1228.5(1)	1203.4(1)
$Z$	1	1
$D_{\text{calc}}$ / g cm <sup>-3</sup>	3.227	3.294
Diffractometer	Bruker APEXII CCD area detector	Bruker APEXII CCD area detector
Radiation type	MoK $\alpha$	MoK $\alpha$
Absorption correction	Numerical	Numerical
$\mu$ / mm <sup>-1</sup>	14.213	14.509
No. of reflections measured	6645	6614
No. of independent reflections	1835	1800
$R_{\text{int}}$	0.0260	0.0231
No. of parameters	78	78
Final $R_1$ values ( $I > 2\sigma(I)$ )	0.0276	0.0214
Final $wR(F^2)$ values ( $I > 2\sigma(I)$ )	0.0524	0.0459
Final $R_I$ values (all data)	0.0417	0.0259
Final $wR(F^2)$ values (all data)	0.0586	0.0476
Goodness of fit of $F^2$	1.066	1.033
Largest diff. peak / eÅ <sup>-3</sup>	0.735	0.569
Largest diff. hole / eÅ <sup>-3</sup>	-1.287	-1.971
CCDC number	999370	999369



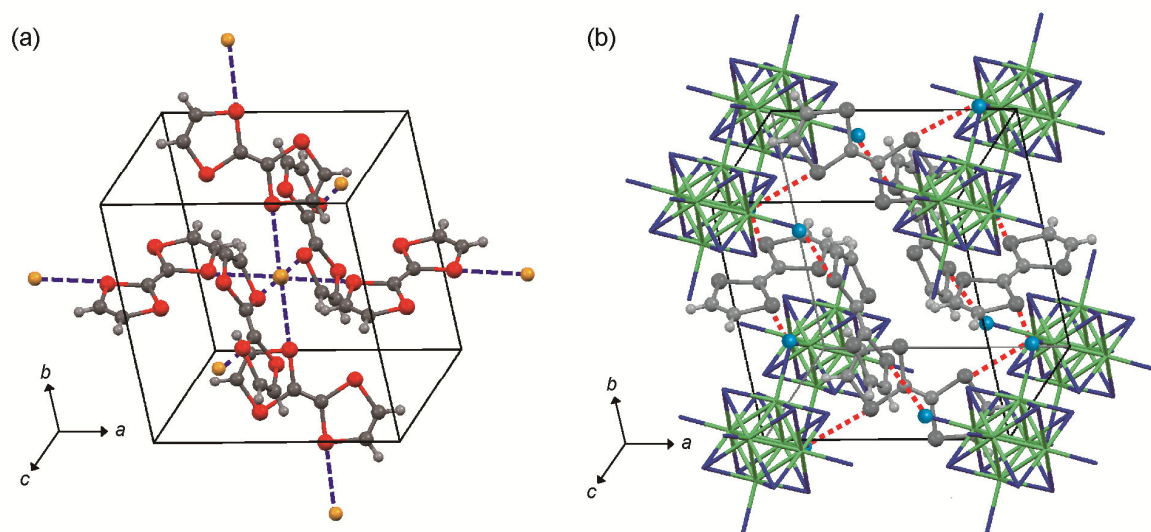


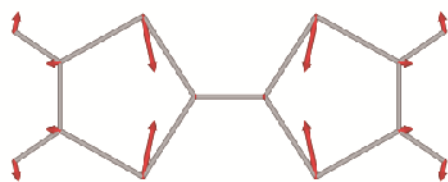
**Fig S1.** Short atomic contacts between chalcogen atoms in TTF or TSF and (a) halogen anion Y (dashed blue line) and (b) apical halogen X<sup>a</sup> in the Mo cluster unit (dashed red line). Gray, dark gray, and orange balls represent hydrogen, carbon, and halogen Y atoms, respectively. Red balls are chalcogen atoms in TTF or TSF. (b) [Mo<sub>6</sub>X<sub>14</sub>] cluster units are depicted in wire frame style (green and blue lines are molybdenum and halogen atoms, respectively). The apical halogens (X<sup>a</sup>) in contact with TTF or TSF in the unit cell are depicted as cyan balls. TTF or TSF molecules are displayed in monochrome.

- Raman spectra of **2** and band assignment

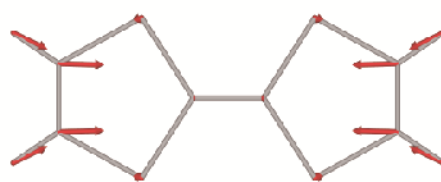
To assign the observed Raman spectra, theoretical calculations were performed using Gaussian 98.<sup>[S1]</sup> Molecular geometry optimization and molecular orbital calculations of TSF<sup>0</sup> and TSF<sup>1+</sup> molecules were carried out using the B3LYP functional with the 6-31G(d,p) basis set, enabling us to calculate normal vibrations. The calculated vibrational frequencies were scaled by a factor 0.9613.<sup>[S2]</sup> The normal vibration modes and these frequencies are summarized in Fig. S2 and Table S4, respectively.

Figure S3 shows the observed Raman spectrum of **2** at 10 K in the range from 200 to 1600 cm<sup>-1</sup>. As the excitation laser (632.8 nm) is not resonant to the electronic transition band of [Mo<sub>6</sub>Br<sub>14</sub>]<sup>2-</sup> (absorption edge: 500 nm),<sup>[S3]</sup> all bands were not derived from [Mo<sub>6</sub>Br<sub>14</sub>]<sup>2-</sup>,<sup>[S4]</sup> but from the TSF molecule (Fig. S9). Observed bands of TSF in **2** and reported bands of TSF<sup>0</sup><sup>[S5]</sup> are summarized in Table S4. Overall, good correspondence was seen for the fundamental modes of a<sub>g</sub>v<sub>6</sub>, a<sub>g</sub>v<sub>5</sub>, a<sub>g</sub>v<sub>3</sub>, and a<sub>g</sub>v<sub>2</sub> between the observed spectrum of **2** and the calculated spectrum of TSF<sup>1+</sup>; however, some differences were seen between 1300 and 1600 cm<sup>-1</sup> (Fig. S4). The a<sub>g</sub>v<sub>3</sub> mode was split in **2** (1395 and 1408 cm<sup>-1</sup>), while no splitting was seen in the calculated spectrum (1373 cm<sup>-1</sup>). This can be ascribed to the factor group splitting in the crystal; however, the origin of the band at 1465 cm<sup>-1</sup> in **2** is currently unknown. The other bands in **2** observed in this range were interpreted by the overtone and combination modes of TSF<sup>1+</sup>, as shown in Table S4. The charge sensitive bands (a<sub>g</sub>v<sub>2</sub>, a<sub>g</sub>v<sub>3</sub>) in the range of 1300 to 1600 cm<sup>-1</sup> showed no significant temperature dependence from 300 to 10 K, as depicted in Fig. S5, indicating that the molecular charge of TSF in **2** did not change from 300 to 10 K.

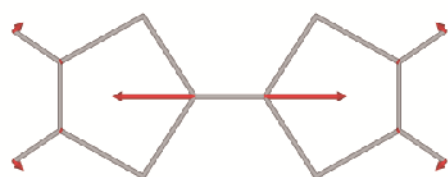
$a_g v_6$  (278)



$a_g v_5$  (582)



$a_g v_3$  (1373)



$b_{1u} v_{14}$  (1487)



$a_g v_2$  (1505)



**Fig. S2.** Typical normal vibration modes of TSF<sup>1+</sup>. The values in parentheses are the calculated wavenumbers of each mode.

**Table S4.** Calculated and observed Raman shifts ( $\text{cm}^{-1}$ ) of TSF

	Observed		Calculated (B3LYP/6-31(d,p))		Evaluated Raman shift of overtone or combination mode from observed fundamental modes
Mode	TSF <sup>0</sup> [S5]	TSF <sup>1+</sup> (2, 10 K)	TSF <sup>0</sup>	TSF <sup>1+</sup>	TSF <sup>1+</sup>
$a_g\nu_6$	272	289	273	278	—
$2 \times a_g\nu_6$	—	576	—	—	578(−2)
$a_g\nu_5$	599*	618	560	582	—
$3 \times a_g\nu_6$	—	865	—	—	867(−2)
$a_g\nu_5 + a_g\nu_6$	—	907	—	—	907(0)
$4 \times a_g\nu_6$	—	1151	—	—	1156(−5)
$a_g\nu_5 + 2 \times a_g\nu_6$	—	1191	—	—	1196(−5)
$a_g\nu_3$	1520	1395	1527	1373	Factor group splitting
		1408			Factor group splitting
$5 \times a_g\nu_6$	—	1440	—	—	1445(−5)
?	—	1465	—	—	—
$b_{1u}\nu_{14}$	—	—	1540	1487	—
$a_g\nu_5 + 3 \times a_g\nu_6$	—	1481	—	—	1485(−4)
$a_g\nu_2$	1549	1515	1553	1505	—

\* Although the  $a_g\nu_5$  mode of TSF<sup>0</sup> was assigned to the band at  $451\text{ cm}^{-1}$  in Ref. S5, we reassigned it to the band at  $599\text{ cm}^{-1}$ , according to our calculation. The values in parentheses represent the difference between observed and evaluated Raman shift wavenumbers of overtone or combination modes.

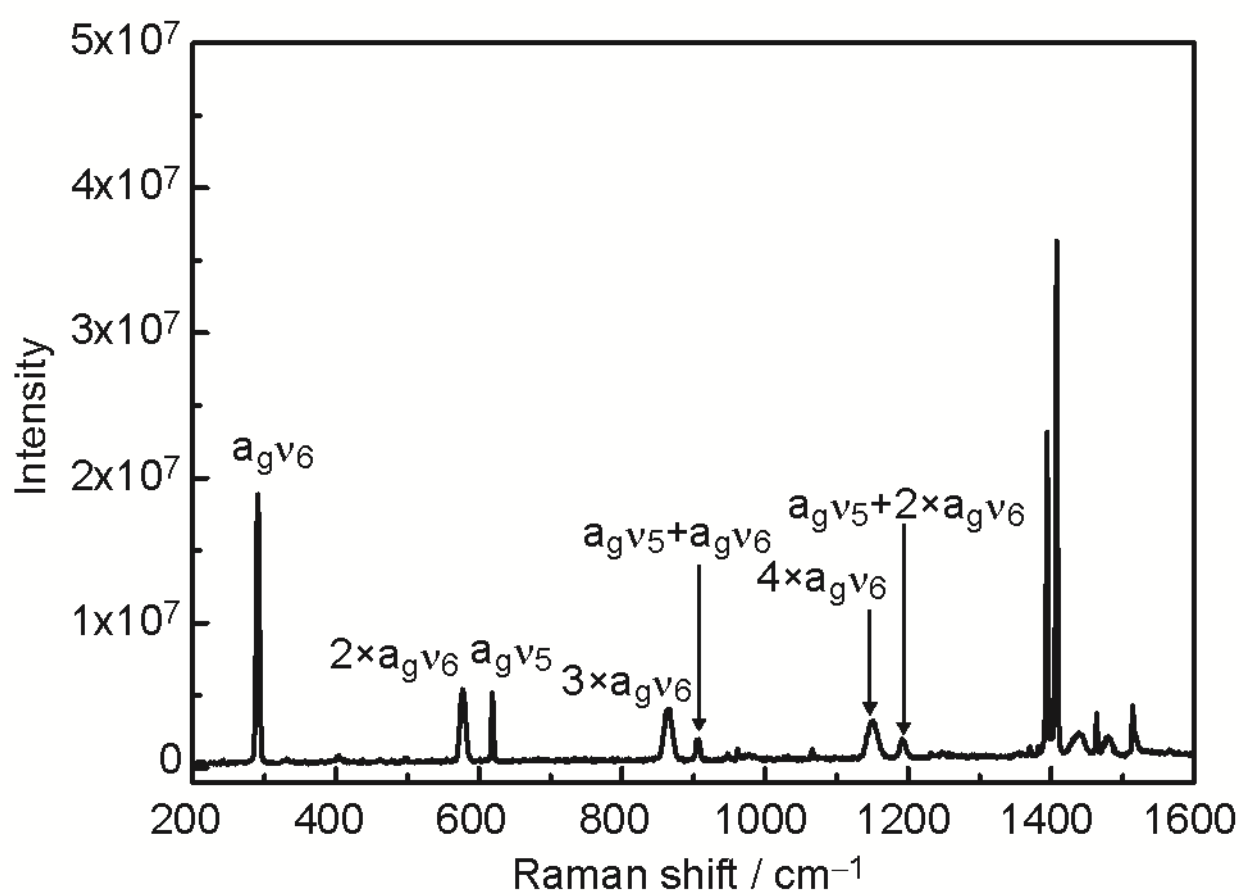
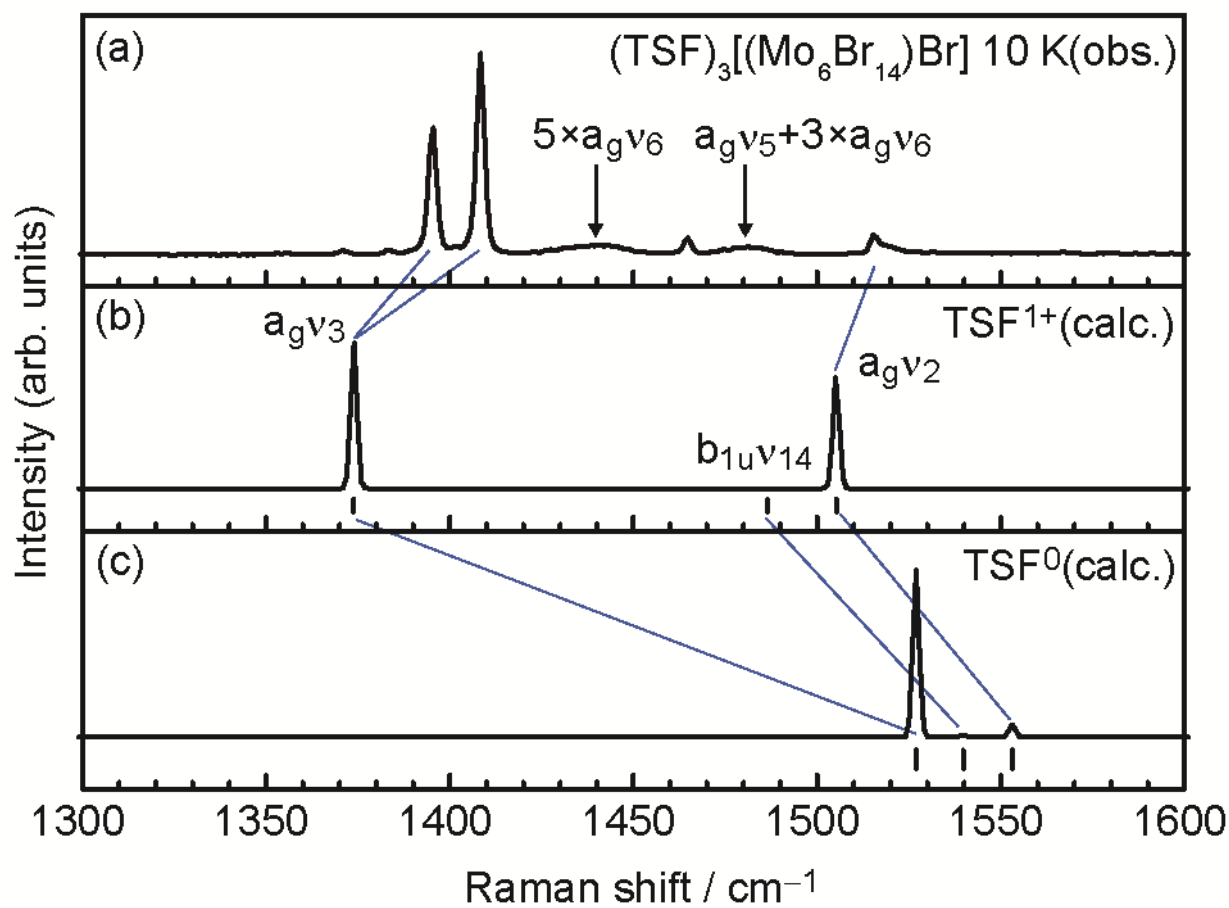
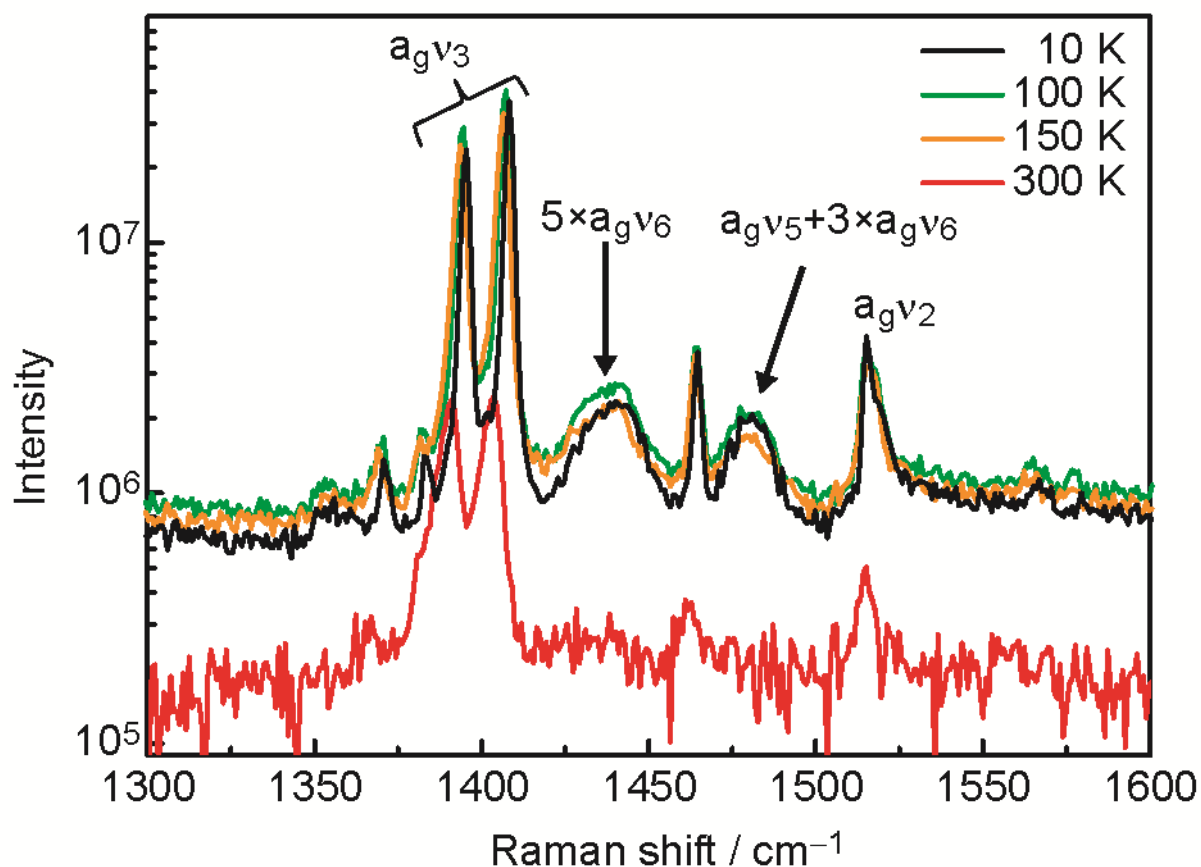


Fig. S3. Raman spectrum of **2** at 10 K.





**Fig. S4.** (a) Raman spectrum of **2** and calculated Raman spectra of (b)  $\text{TSF}^{1+}$  and (c)  $\text{TSF}^0$ . In (b) and (c), the black vertical bars under the calculated spectra indicate the calculated wavenumber of the normal vibration modes. The blue lines indicate the assignment of each band. The calculated Raman shifts of  $\text{TSF}^0$  correspond well to the reported shifts (Table S4).<sup>[S5]</sup>



**Fig. S5.** Temperature dependence of the Raman spectra (300–10 K, 1300–1600  $\text{cm}^{-1}$ ). With the exception of the intensity of overtone and combination bands, the charge sensitive vibration modes ( $a_g v_2$ ,  $a_g v_3$ ) did not show any significant change between 300 and 10 K.

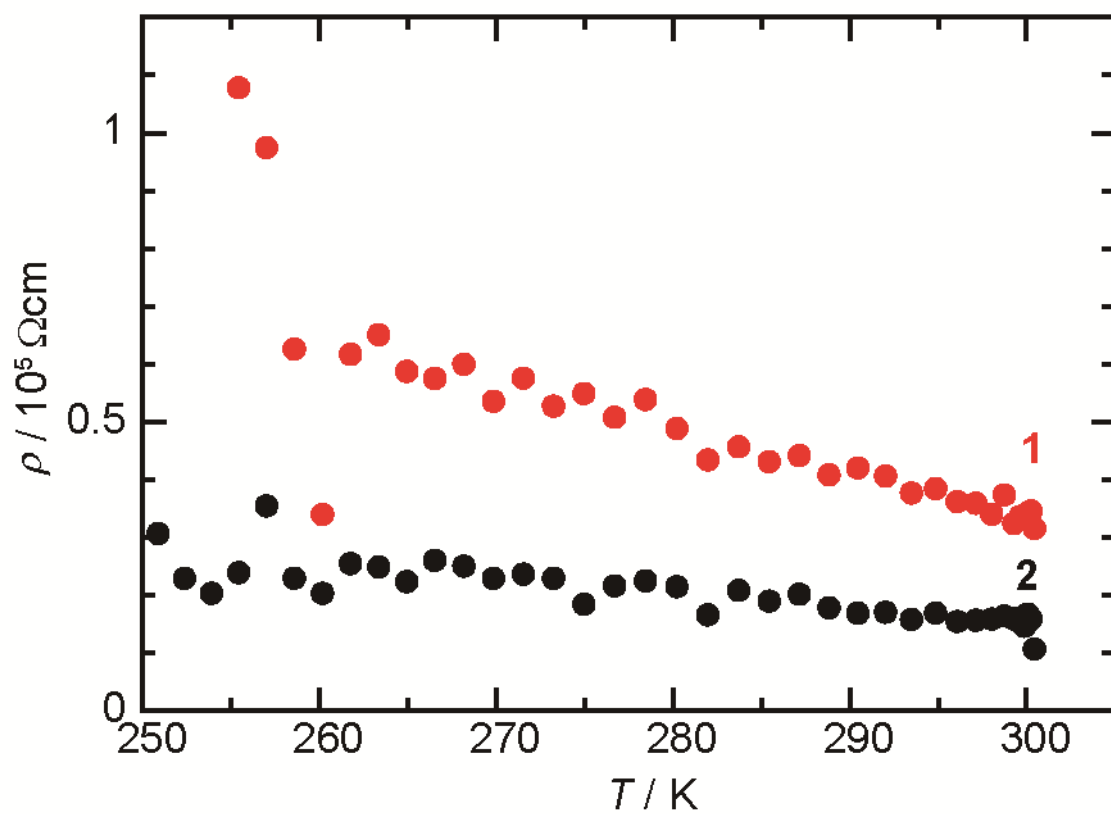


**Fig S6.** Temperature dependence of the resistivity of **1** (red circles) and **2** (black circles).

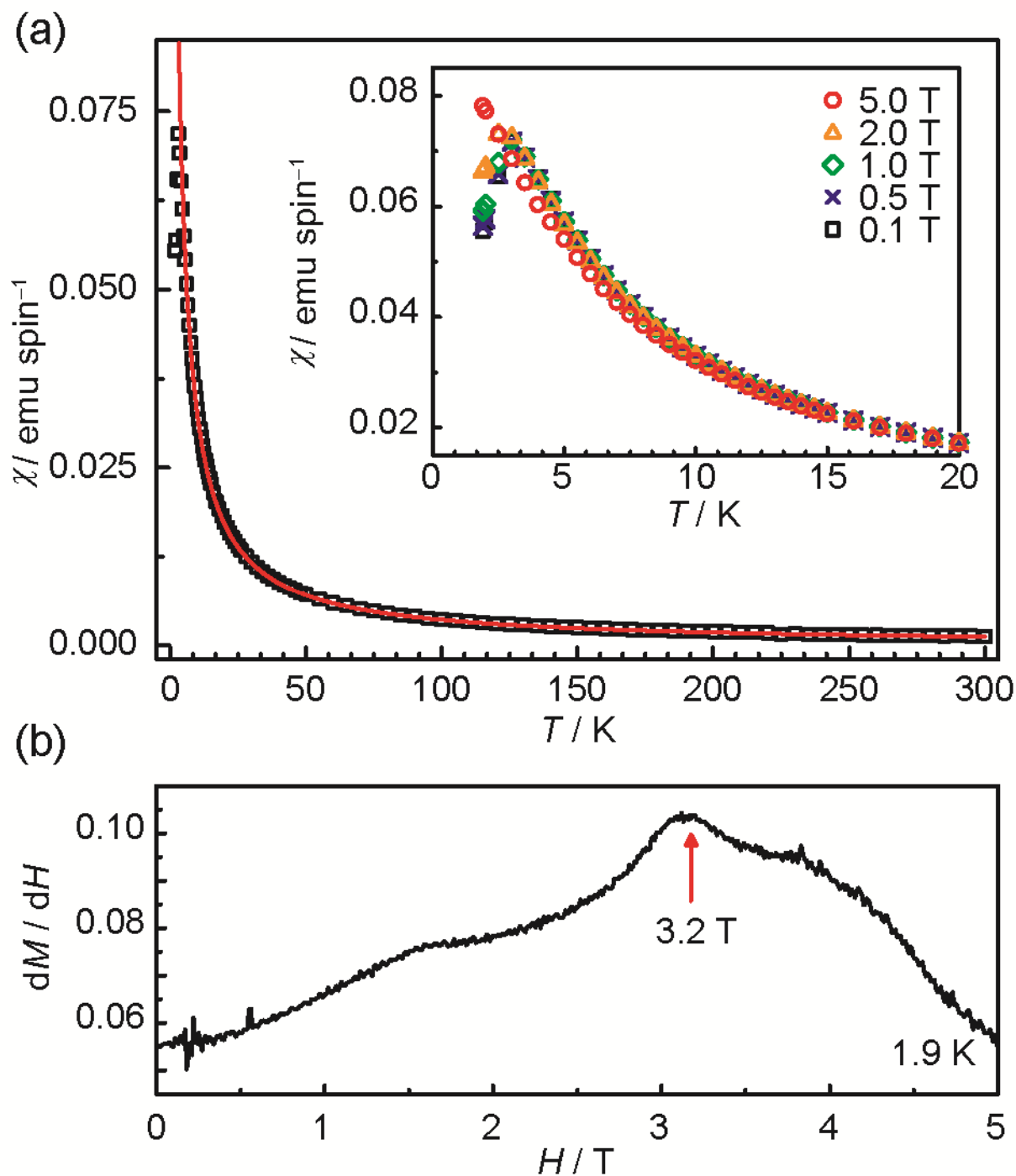


**Fig S7.** (a) Temperature dependence of the static magnetic susceptibility of **1** (polycrystals) at 0.1 T. Solid red line is the Curie-Weiss fit with  $C = 0.370 \text{ emu K mol}^{-1}$  and  $\Theta_{\text{CW}} = -1.6 \text{ K}$ . Inset shows the magnetic field dependence (0.1–5.0 T) of  $\chi$  below 20 K. (b)  $dM/dH$  at 1.9 K. A scatter of  $dM/dH$  at the region of  $H = 0.10\text{--}0.45 \text{ T}$  resulted from inherent properties of the superconducting magnet. Red arrow indicates the spin-flop magnetic field.

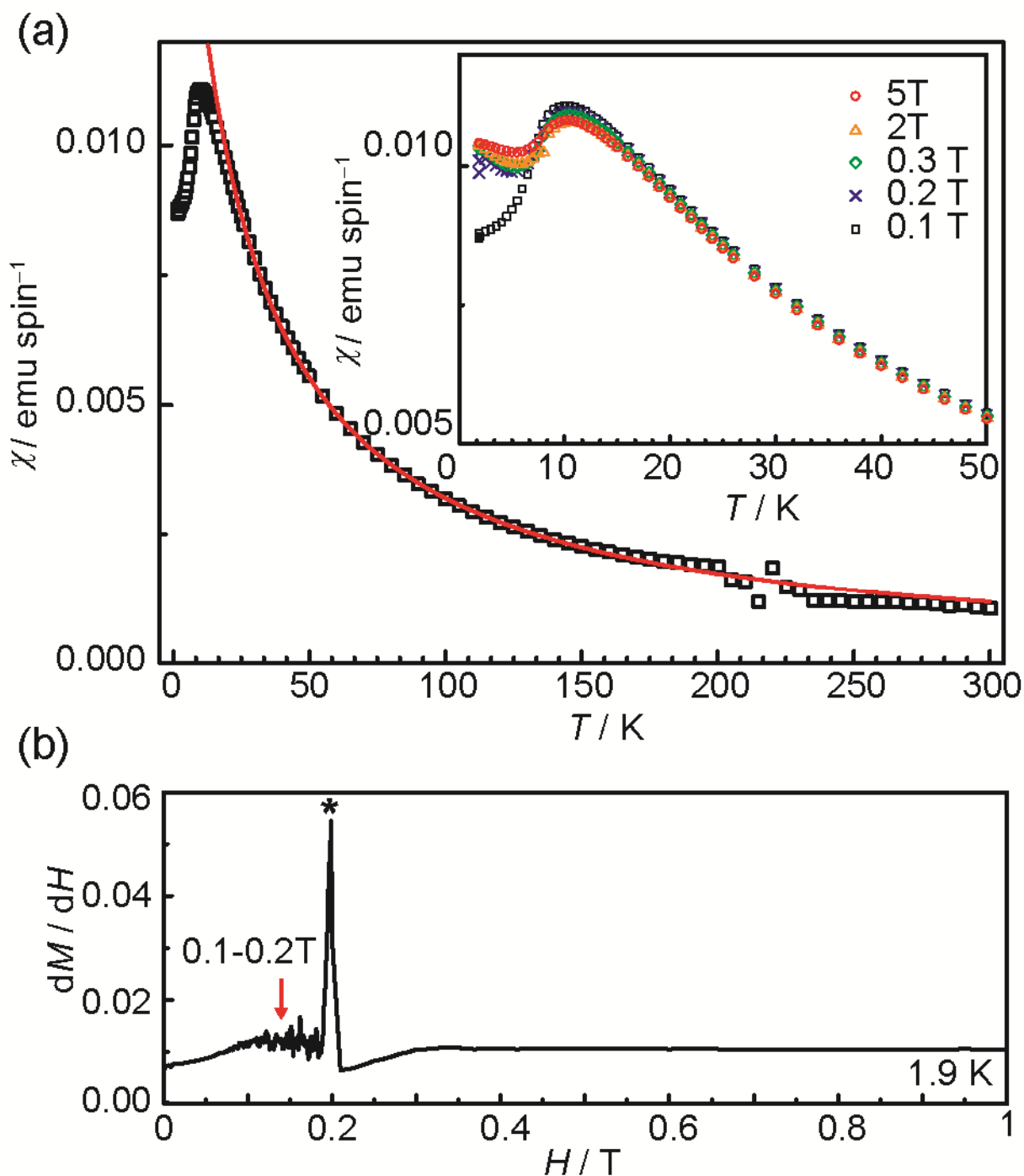


**Fig S8.** (a) Temperature dependence of the static magnetic susceptibility of  $(\text{TTF})_3[(\text{Mo}_6\text{Br}_{14})\text{Br}]$  (polycrystals) at 0.1 T. Solid red line is the Curie-Weiss fit with  $C = 0.381 \text{ emu K mol}^{-1}$  and  $\Theta_{\text{CW}} = -19.0 \text{ K}$ . Inset shows the magnetic field dependence (0.1–5.0 T) of  $\chi$  below 50 K. (b)  $dM/dH$  at 1.9 K. A scatter of  $dM/dH$  at the region of  $H = 0.10$ – $0.45 \text{ T}$  resulted from inherent properties of the superconducting magnet. The peak at 0.2 T indicated by \* is also thought to the same origin; therefore, the spin flop magnetic field is deduced to be 0.1–0.2 T, as indicated by the red arrow.



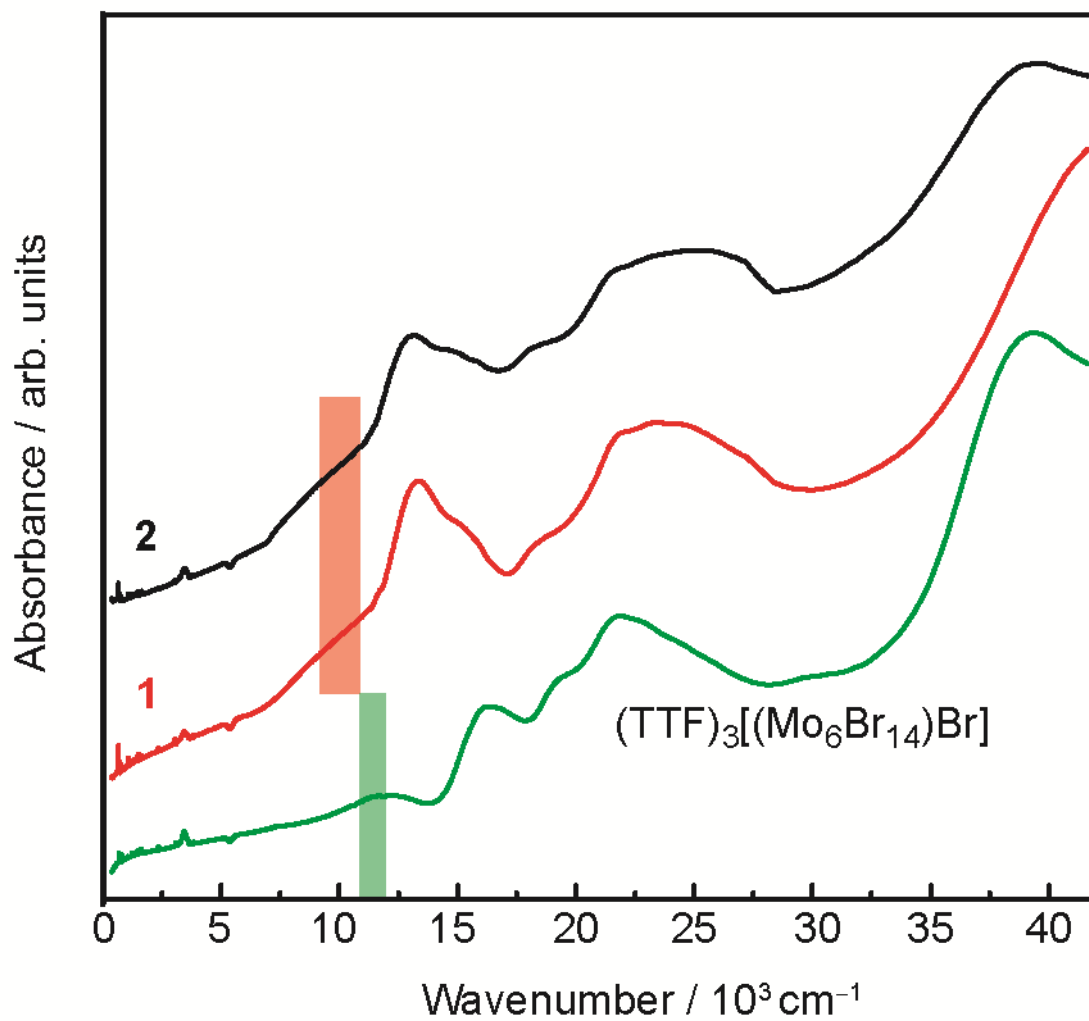


**Fig S9.** Optical absorption spectra of (TTF)<sub>3</sub>[(Mo<sub>6</sub>Br<sub>14</sub>)Br] (green line), **1** (red line), and **2** (black line). The estimated peaks positions of the first CT absorption band are indicated by the red zone (1.2–1.4 eV) for **1** and **2** and the green zone (1.4–1.5 eV) for (TTF)<sub>3</sub>[(Mo<sub>6</sub>Br<sub>14</sub>)Br].

## References

- S1. M. J. Frisch, G. W. Trucks, H. B. Schlegel, G. E. Scuseria, M. A. Robb, J. R. Cheeseman, V. G. Zakrzewski, J. A. Montgomery, Jr., R. E. Stratmann, J. C. Burant, S. Dapprich, J. M. Millam, A. D. Daniels, K. N. Kudin, M. C. Strain, O. Farkas, J. Tomasi, V. Barone, M. Cossi, R. Cammi, B. Mennucci, C. Pomelli, C. Adamo, S. Clifford, J. Ochterski, G. A. Petersson, P. Y. Ayala, Q. Cui, K. Morokuma, N. Rega, P. Salvador, J. J. Dannenberg, D. K. Malick, A. D. Rabuck, K. Raghavachari, J. B. Foresman, J. Cioslowski, J. V. Ortiz, A. G. Baboul, B. B. Stefanov, G. Liu, A. Liashenko, P. Piskorz, I. Komaromi, R. Gomperts, R. L. Martin, D. J. Fox, T. Keith, M. A. Al-Laham, C. Y. Peng, A. Nanayakkara, M. Challacombe, P. M. W. Gill, B. Johnson, W. Chen, M. W. Wong, J. L. Andres, C. Gonzalez, M. Head-Gordon, E. S. Replogle, J. A. Pople, Gaussian 98, Revision A.11.2, Gaussian, Inc., Pittsburgh PA, 2001.
- S2. M. W. Wong, *Chem. Phys. Lett.*, 1996, **256**, 391-399.
- S3. A. W. Maverick, J. S. Najdzionek, D. MacKenzie, D. G. Nocera, H. B. Gray, *J. Am. Chem. Soc.*, 1983, **105**, 1878-1882.
- S4. J. R. Schoonover, T. C. Zietlow, D. L. Clark, J. A. Heppert, M. H. Chisholm, H. B. Gray, A. P. Sattelberger, W. H. Woodruff, *Inorg. Chem.*, 1996, **35**, 6606-6613.
- S5. K. Iwahana, H. Kuzmany, F. Wudl, E. A.-Shalom, *Mol. Cryst. Liq. Cryst.*, 1982, **79**, 39-47.

**Statement to specify the contribution of each co-author**

- Takaaki Hiramatsu: Synthesis of complexes **1**, **2**,  $(\text{TTF})_3[(\text{Mo}_6\text{Br}_{14})\text{Br}]$ , X-ray structure analysis, transfer integrals calculation, UV-VIS-NIR measurements, theoretical calculation for normal vibration mode analysis, band assignments of Raman spectra and manuscript preparation
- Yukihiro Yoshida: Synthesis of complex **2**, X-ray structural analysis of **2** (100-298 K) and transfer integrals calculation of some complexes
- Gunzi Saito: Design of the study and manuscript preparation
- Akihiro Otsuka: SQUID and EPR measurements
- Hideki Yamochi: SQUID and EPR measurements
- Yasuhiro Shimizu: NMR measurements
- Yuma Hattori: Raman measurements
- Yuto Nakamura: Raman measurements and band assignments of Raman spectra
- Hideo Kishida: Raman measurements and band assignments of Raman spectra
- Hiroshi Ito: direct current conductivity measurements
- Kaplan Kirakci: Synthesis of Mo clusters
- Stéphane Cordier: Synthesis of Mo clusters
- Christiane Perrin: Synthesis of Mo clusters

Corrigenda

	Reads	Change to
p. 1, Affiliation d	<i>Nagoya University, Nagoya 464-8602, Japan</i>	<i>Nagoya University, Chikusa-ku, Nagoya 464-8602, Japan</i>
p. 2, l. 8 from the bottom	Only the QSL state of $\kappa$ -(ET) <sub>2</sub> Cu <sub>2</sub> (CN) <sub>3</sub> neighbors to superconducting state among them.	Among them, $\kappa$ -(ET) <sub>2</sub> Cu <sub>2</sub> (CN) <sub>3</sub> is unique in that the QSL phase neighbors to the superconducting phase under pressure.
Caption in Fig. 3	face-capped	face-capping
p. 3, l. 3	TBA•Y	(TBA)Y
p. 3, l. 6	TBA•X	(TBA)X
Caption in Fig. 4	Crystal structure of (TSF <sup>+</sup> ) <sub>3</sub> [(Mo <sub>6</sub> Br <sub>14</sub> <sup>2-</sup> )Br <sup>-</sup> ] ( <b>2</b> ) depicted in ball and stick style. TSF molecules and bromine anion are depicted as balls (gray, ... atoms, respectively.) [Mo <sub>6</sub> Br <sub>14</sub> ] cluster units ...	Crystal structure of (TSF <sup>+</sup> ) <sub>3</sub> [(Mo <sub>6</sub> Br <sub>14</sub> <sup>2-</sup> )Br <sup>-</sup> ] ( <b>2</b> ). TSF molecules and bromine anions are depicted in the ball and stick style (gray, ... atoms, respectively), whereas [Mo <sub>6</sub> Br <sub>14</sub> ] cluster units ...
Caption in Fig. 6	dM <sub>p</sub> /dH	dM/dH
4th column in Table 3	$\theta_{\text{CW}}/K$	$\theta_{\text{CW}}/K$
Ref. 19	<b>304 n°18</b>	<b>304</b>